

1 Long-term monitoring (1953-2019) of geomorphologically active 2 sections of Little Ice Age lateral moraines in the context of changing 3 meteorological conditions

4 Moritz Altmann¹, Madlene Pfeiffer², Florian Haas¹, Jakob Rom¹, Fabian Fleischer¹, Tobias Heckmann¹,
5 Livia Piermattei^{1,3}, Michael Wimmer⁴, Lukas Braun⁵, Manuel Stark¹, Sarah Betz-Nutz¹, Michael Becht¹

6 ¹Department of Physical Geography, Catholic University of Eichstätt-Ingolstadt, Eichstätt, 85072, Germany

7 ²Institute of Geography, University of Bremen, Bremen, 28359, Germany

8 ³Swiss Federal Institute for Forest, Snow and Landscape Research (WSL), Birmensdorf, 8903, Switzerland

9 ⁴Department of Geodesy and Geoinformation, TU Wien, Vienna, 1040, Austria

10 ⁵Institute of Mathematics, Albert Ludwig University of Freiburg, Freiburg, 79104, Germany

11 *Correspondence to:* Moritz Altmann (MAltmann@ku.de)

12 **Abstract.** We show a long-term erosion monitoring of several geomorphologically active gully systems on Little Ice Age
13 lateral moraines in the European Central Eastern Alps covering a total time period from 1953 to 2019 including several survey
14 periods in order to identify corresponding morphodynamic trends. For the implementation, DEM of Differences were
15 calculated based on multitemporal high-resolution digital elevation models from historical aerial images (generated by
16 structure-from-motion photogrammetry with multi-view-stereo) and light detection and ranging from airborne platforms. Two
17 approaches were implemented to achieve the corresponding objectives. First, by calculating linear regression models using the
18 accumulated sediment yield and the corresponding catchment area (on a log-log scale), the range of the variability of the spatial
19 distribution of erosion values within the sites. Secondly, we use volume calculations to determine the total/mean sediment
20 output (and erosion rates) of the entire sites. Subsequently, both the sites and the different time periods of both approaches are
21 compared. Based on the slopes of the calculated regression lines, it can be shown that the highest variability of sediment yield
22 in the sites occurs in the first time period (mainly 1950s to 1970s). This can be attributed to the fact that within some sites the
23 sediment yield per square metre increases clearly more strongly (regression lines with slopes up to 1.5). In contrast, in the later
24 time periods (1970s to mid-2000s and mid-2000s to 2017/2019), there is generally a decrease in 10 out of 12 cases (regression
25 lines with slopes around 1). However, even in the sites with an increase in the variability of sediment yield over time, the
26 earlier high variabilities are no longer reached. This means that the spatial pattern of erosion in the gully heads changes over
27 time as it becomes more uniform. Furthermore, using sediment volume calculations and corresponding erosion rates, we show
28 a generally decreasing trend in geomorphic activity (amount of sediment yield) between the different time periods in 10 out of
29 12 sites, while 2 sites show an opposite trend where morphodynamics increase and remain at the same level. Finally, we
30 summarise the results of long-term changes in the morphodynamics of geomorphologically active areas on lateral moraines by
31 presenting the "sediment activity concept", which, in contrast to theoretical models, is based on actually calculated erosion.
32 The level of geomorphic activity depends strongly on the characteristics of the sites, such as size, slope length and slope

33 gradient, some of which are associated with deeply incised gullies. It is noticeable that especially areas with influence of dead
34 ice over decades in the lower slope area show high geomorphic activity. Furthermore, we show that system-internal factors as
35 well as the general paraglacial adjustment process have a greater influence on long-term morphodynamics than changing
36 external weather and climate conditions, which, however, had a slight impact mainly in the last, i.e. most recent time period
37 (mid-2000s to 2017/2019) and may have led to an increase in erosion at the sites.

38 **Keywords:** Airborne Laser Scanning (ALS), DEM of Difference (DoD), gully erosion, historical aerial images, Little Ice Age
39 (LIA) lateral moraines, paraglacial process system, proglacial areas, Structure-from-Motion (SfM) photogrammetry, Weather
40 Research and Forecasting (WRF) model

41 **1 Introduction**

42 Since the end of the Little Ice Age (LIA) around 1850 (Matthews and Briffa, 2005; Ivy-Ochs et al., 2009) and the strong global
43 warming of the last decades (IPCC, 2021; Pepin et al., 2022), proglacial areas play a special role in the current landscape
44 changes of high alpine geosystems, as such areas are strongly extending due to the ongoing retreat of the glaciers (Deline et
45 al; Heckmann and Morche, 2019; Haeberli and Whiteman, 2021). The melting of glaciers leads to the release of unstable
46 sediment sources, which are subsequently exposed to several geomorphological slope processes, which can lead to high erosion
47 rates.

48 The relationship between this glacier melt and slope instability has been subject of research for several decades. Church and
49 Ryder (1972) were the first to develop a theoretical model (“paraglacial concept”) to describe future landscape change
50 throughout a proglacial area and defined the phase of transition as the paraglacial period, during which paraglacial processes
51 (non-glacial processes) occur. After a period of high geomorphic activity (fluvial erosion and transport) associated with a peak,
52 sediment production decreases over time until a “normal” level of sediment movement is reached. By further developing the
53 model, Ballantyne (2002a) describes this paraglacial landscape adjustment using the “sediment exhaustion model”, which is
54 based on a hypothetical paraglacial system. Several variable factors determine the duration of this period, such as sediment
55 release and the rate of sediment reworking. Following the sediment exhaustion model, the rate of sediment reworking of
56 glacial sediments in proglacial areas decreases exponentially if the sediment release rate only depends on sediment
57 availability (Ballantyne, 2002a, 2002b).

58 Ballantyne and Benn (1994) and Curry (1999) describe the paraglacial slope adjustment of lateral moraines by analysing the
59 formation of gully systems on lateral moraines and the corresponding alluvial fans and debris cones (both in western Norway).
60 These systems result from weathering and erosion, such as fluvial erosion, slope wash, debris flows, smaller slope failures,
61 and ground/snow avalanches (Ballantyne, 2002a, 2002b; Curry et al., 2006; Haas et al., 2012; Dusik et al., 2019). Material is
62 deposited in the gullies (e.g. by nival processes, fluvial activity and sidewall collapse) and subsequently transported downslope,
63 mainly by debris flows triggered in the gully heads after heavy rainfall or after rapid snowmelt (Ballantyne and Benn, 1994;
64 Ballantyne, 2002b; Curry et al., 2006). Similarly, large deformations such as deep-seated slope failures and landslides with

65 low frequency and high magnitude also occur (Mattson and Gardner, 1991; Blair, 1994; Hugenholtz et al., 2008; Altmann et
66 al., 2020; Cody et al., 2020; Betz-Nutz, 2021; Zhong et al., 2022). These erosion processes are primarily driven by temperature
67 and precipitation events, which have been subject to change in recent years and decades (Serquet et al., 2011; Brugnara et al.,
68 2012; Mankin and Diffenbaugh, 2015; Klein et al., 2016; Beniston et al., 2018; Hock et al., 2019; IPCC, 2021; Pepin et al.,
69 2022). Spring-time snowmelt provide important preparatory steps for sediment transport processes, such as loosening of the
70 upper layers of sediments of the slope or through the delivery of material into the gullies by nival processes, which is then
71 transported downslope by debris flows in the summer months (Haas et al., 2012; Dusik et al., 2019), which is considered as
72 the most important process occurring (Ballantyne, 2002a; Curry et al., 2006). Dusik (2019) also shows a positive correlation
73 between the number of mass movements and the number of extreme precipitation intensities, the number of certain threshold
74 exceedances for extreme daily precipitation totals as well as annual precipitation totals. These processes ultimately lead to the
75 dissection of the upper parts of the lateral moraines which is, however, limited in time (Curry et al., 2006). Curry et al. (2009)
76 inferred from morphometric measurements along a chronosequence that gullies increase in depth, width, area, and volume
77 over time, with width increasing significantly more than depth, resulting in the older ones not being as densely gullied.
78 Furthermore, it is described that the slope gradient decreases over time, e.g. Ballantyne and Benn (1994) report an average of
79 5° (in 48 years between 1943 and 1991). Betz-Nutz et al. (2023) document a range of slope gradient changes between -3.2°
80 and $+6.6^\circ$ between the ~1950s and 2018 (~68 years), showing that both increases and decreases can occur. Ballantyne and
81 Benn (1994), Curry (1999) and Curry et al. (2006) give average annual erosion rates of different gully systems over several
82 decades estimated by the volume of the gullies. Curry et al. (2006) showed at different test sites in the Swiss Alps that the
83 maximum extent of gullies is reached after 50 years of ice release and that sediment filling and stabilisation occurs after 80-
84 140 years of deglaciation. While 50% of the available sediment is exhausted after 10-50 years, it can take several centuries
85 until the paraglacial adjustment process is completed (Curry et al., 2006). Schiefer and Gilbert (2007) show, based on
86 quantitative analyses (via stereo-photogrammetry using historical aerial images), a significant decrease in the geomorphic
87 activity of gully systems on lateral moraines over several decades and different time periods in the glacier foreland of the
88 Lillooet Glacier (Canada, British Columbia). Carrivick et al. (2013) generally confirm the concept of paraglacial adjustment
89 by showing decreasing morphodynamics with increasing distance from the glacier as they have been ice-free for a longer time.
90 However, the lower morphodynamics observed in the distal areas of the glacier forelands could also be due to the generally
91 lower slope gradients there (Betz-Nutz et al., 2023). Lane et al. (2017) showed in the glacier foreland of Haut Glacier d'Arolla
92 (Switzerland, Valais) that there are no indications of filling in the developed gully systems, which indicates that they are still
93 in the incision phase. Betz-Nutz et al. (2023) show with the use of historical aerial photographs (processed by SfM-
94 photogrammetry) that the paraglacial adjustment process over decades is very variable. While 13 out of 20 moraine sections
95 showed decreasing erosion rates over decades, divided into several time periods, six showed almost constant activity and one
96 section even showed a substantial increase in erosion rate.

97 The period of paraglacial landscape adjustment is also influenced by upcoming vegetation, which can be considered both a
98 consequence and a cause of slope stabilisation (Eichel et al., 2016; Haselberger et al., 2021; Haselberger et al., 2022; Eichel et

99 al., 2023). Nevertheless, bound solifluction processes can occur under a dense vegetation cover and are therefore not an
100 absolute sign of stabilisation (Dracbing and Eichel, 2017).

101 The generation of multitemporal accurate and precise digital elevation models (DEMs) and the resulting DEM of Differences
102 (DoDs) by different remote sensing methods and techniques, which have been established in geomorphological research in
103 recent years, enabled the detection of changes in the Earth's surface in high spatial and temporal resolution (Pulighe and Fava,
104 2013; Nebiker et al., 2014; Tarolli, 2014; Smith et al., 2016; Eltner et al., 2016; Sevara et al., 2018; Okyay et al., 2019; Noto
105 et al., 2017). By processing overlapping high-resolution digitised historical aerial images of high alpine geosystems, using
106 SfM-MVS (Structure-from Motion with Multi-View-Stereo) digital stereo-photogrammetry in combination with current
107 airborne LiDAR (Light Detection And Ranging) data into DEMs and the corresponding DoDs, landscape changes in these
108 areas can be reconstructed over several decades (Midgley and Tonkin, 2017; Mölg and Bolch, 2017; Lane et al., 2017; Betz et
109 al., 2019; Altmann et al., 2020; Fleischer et al., 2021; Betz-Nutz, 2021; Stark et al., 2022; Piermattei et al., 2022). The spatial
110 distribution of positive and negative DoD elevation changes enable various analyses, such as the reconstruction and
111 interpretation of individual geomorphological processes (Dusik, 2019) or the calculation of morphological budgets (Altmann
112 et al., 2020).

113 Furthermore, by applying flow routing algorithms and the accumulation of DoD values accordingly, sediment yield from the
114 contributing area of each cell can be determined: Pelletier and Orem (2014) used repeat airborne LiDAR-based DEMs before
115 and after a wildfire and calculated for each pixel the net sediment volume exported by geomorphological processes. Further
116 applications of this methodology have been published by Wester et al. (2014), who calculated the total sediment yield by
117 applying a weighted flow accumulation algorithm, and Heckmann and Vericat (2018), who further developed the approach by
118 calculating a spatially distributed measure of functional sediment connectivity on a proglacial slope. Neugirg et al. (2015a;
119 2015b; 2016) showed a positive correlation between log sediment yield (calculated by accumulated DoD values on slopes)
120 and the corresponding log sediment contributing area, respectively log catchment area (using the sediment-contributing-area
121 approach), both extracted at randomly selected cells of the channel network (so-called "virtual sediment traps"). Besides to
122 these studies conducted over several months and years on slopes in the Northern Alps (Germany, Lainbach valley and Arzbach
123 valley) and at a former iron ore mine on the island of Elba in the Tyrrhenian Sea (Italy, next to Rio Marina)), this approach
124 was also applied by Dusik (2019) and Dusik et al. (2019) over several weeks to a proglacial slope in Kaunertal (Austria, Tyrol).

125 One advantage of this approach is that it can be used to determine not only the size of sediment yield (which can be compared
126 with previous time periods, for example), but also the variability of sediment yield within the site in an time period (spatial
127 pattern of sediment yield within the site), which is not possible, for example, when calculating simple erosion rates, where
128 only the volume of the total change can be computed.

129 In this study we apply the sediment-contribution-area approach to several LIA lateral moraine sections over several decades
130 and several time periods in the European Central Eastern Alps in order to better understand the paraglacial adjustment process
131 of lateral moraines. Thus, the aim is to find out how the spatial erosion pattern within the areas changes over time. Secondly,
132 we show volume calculations of the entire sites to determine the total sediment yield (and erosion rates). Therefore, by

133 combining high-resolution historical and current DEMs and the corresponding DoDs, we show quantification and analysis of
 134 gully system morphodynamics at 12 different sections in the upper reaches of lateral moraines in five different glacier forelands
 135 over a total period of several decades (1953-2019) with several survey periods (~1950s to ~1970s, ~1970s to ~2000s and
 136 ~2000s to 2017/2019). By using simulated climate data of the glacier forelands we were able to investigate, besides system-
 137 internal influences, also external impacts on the morphodynamics, which have not been considered in long-term studies on
 138 erosion of LIA lateral moraines so far.

139 2 Study Area

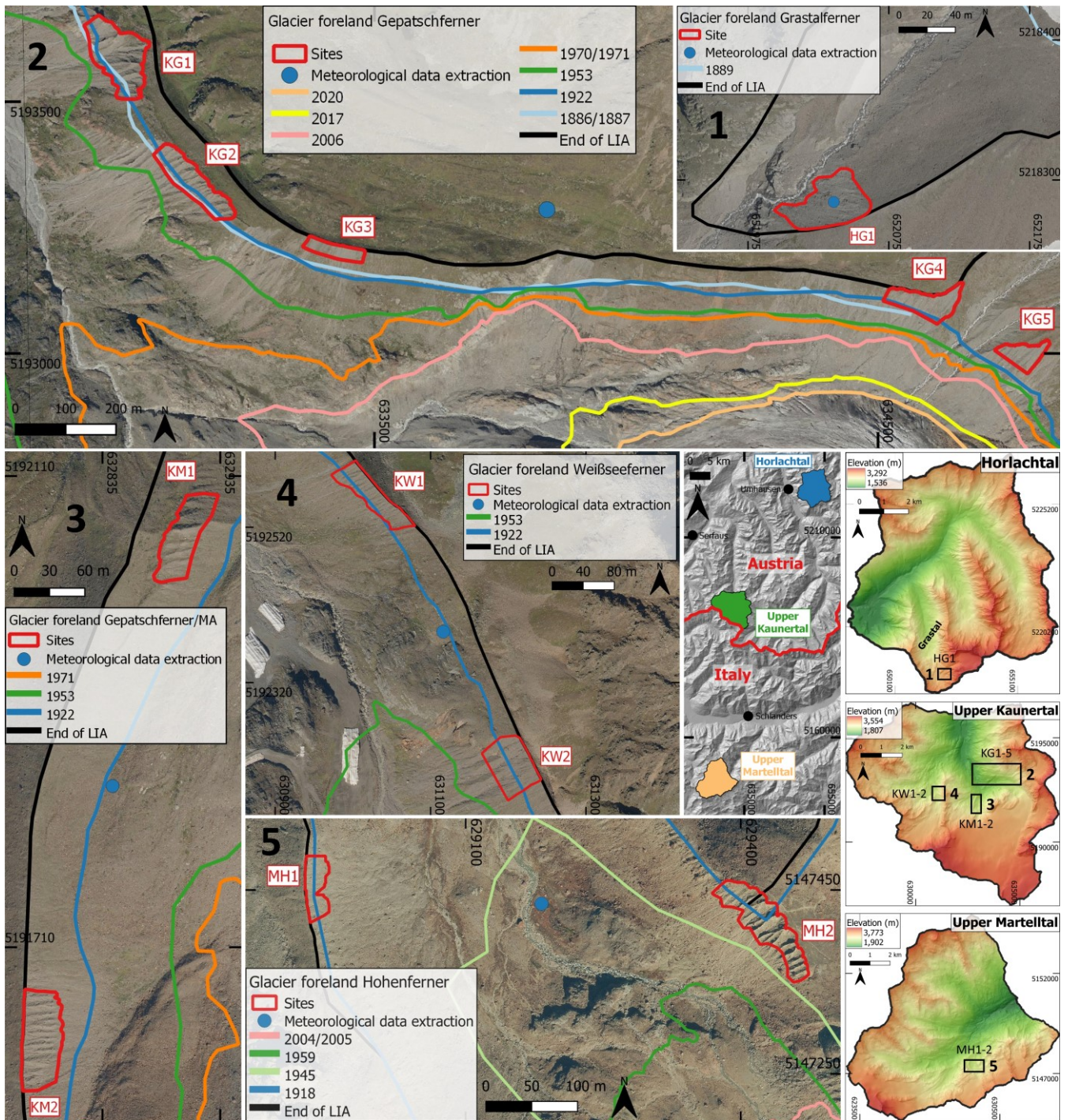
140 The sites are located in different high alpine geosystems along a north-south axis in the European Central Eastern Alps and
 141 are situated north (Horlachtal and upper Kaunertal) and south (upper Martelltal) of the Main Alpine Divide. In these valleys,
 142 the sites are located within five glacier forelands on lateral moraines formed by the glaciers during their maximum glacier
 143 outline during the LIA around 1850 (Figure 1). The Horlachtal is located in the Stubai Alps (Tyrol, Austria), which is a tributary
 144 of the Oetztal (Geitner, 1999; Rieger, 1999). The investigated section of the Horlachtal is located in the side valley and sub-
 145 catchment Grastal (glacier foreland Grastalferner), which is oriented in a north-south direction. Geologically, the Horlachtal
 146 is located in the Oetztal Massif, where gneisses and mica schists dominate (Becht, 1995; Geitner, 1999). The Kaunertal is also
 147 located in the Oetztal Alps (Tyrol, Austria) and is oriented in a north-south direction. This valley geologically belongs to the
 148 Austroalpine crystalline complex (Tollmann, 1977; Geological Survey of Austria, 1999) where crystalline rocks, mainly ortho-
 149 and paragneisses, dominate (Vehling, 2016). The sites within the Kaunertal are located in the glacier forelands of the
 150 Gepatschferner, another glacier outlet of the Gepatschferner, the so-called Münchner Abfahrt (MA), and the Weißseeferner.
 151 The Martelltal is a southwest-northeast oriented valley located in the Ortler-Cevedale group (South Tyrol, Italy) and belongs
 152 geologically to the Ortler-Campo Crystalline, where quartz phyllite dominates with layers of e.g. shales, gneisses and marbles
 153 (Mair and Purtscheller, 1996; Staindl, 2000; Mair et al., 2007). The two sites are located in the glacier foreland of the
 154 Hohenferner. All valleys are characterized by the continental climate and low annual precipitation sums of the inner alpine dry
 155 region (Becht, 1995; Hagg and Becht, 2000; Veit, 2002; Hilger, 2017; Betz-Nutz, 2021). The sites are characterized by very
 156 sparse vegetation cover, intense paraglacial morphodynamics and typical unsorted moraine material. Table 1 and Figure 1 give
 157 an overview of the location as well as the characteristics of the sites.

158 **Table 1: Characteristics of the sites. Values were derived from 2017 DEM (Kaunertal) and 2019 DEM (Horlachtal and Martelltal).**

Sites	Location (Centre) (ETRS89/ UTM Zone 32N, EPSG Code: 25832)	Elevation (Ellipsoidal heights) (m)	Aspect	Size (m ²)	Max. length of delineated site (downslope) (m)	Mean (and max.) slope gradient (°)	At least ice- free since (years)*	Glacial or dead ice influence at the foot of the slope
HG1	E 652032, N 5218283	2659-2696	W	1647	43	37.9 (46.8)	1860 (159)	Not detectable
KG1	E 632991, N 5193590	2183-2262	W	12431	124	41.5 (69.3)	1937 (80)	Not detectable

KG2	E 633140, N 5193339	2244-2321	SW	8814	59	43.8 (61)	1933 (84)	Until 2006
KG3	E 633421, N 5193204	2329-2400	S	3123	29	38.5 (48.3)	1872 (145)	Not detectable
KG4	E 634596, N 5193101	2540-2620	SW	6193	99	41.1 (61.3)	1929 (88)	until today
KG5	E 634789, N 5192997	2580-2645	SW	3531	77	44.3 (57.1)	1913 (104)	until today
KM1	E 632904, N 5192058	2443-2486	E	2025	23	39.8 (46.9)	1903 (114)	Not detectable
KM2	E 632783, N 5191632	2560-2598	E	2534	30	45.7 (56.7)	1901 (116)	Until 2006
KW1	E 631025, N 5192561	2546-2603	SW	2951	38	41.6 (54.4)	1924 (93)	Not detectable
KW2	E 631204, N 5192213	2682-2714	SW	3638	49	39.9 (53.4)	1937 (80)	Until 2006
MH1	E 628937, N 5147454	2704-2729	E	1475	26	35.5 (51.6)	1921 (98)	Not detectable
MH2	E 629426, N 5147413	2755-2796	SW	3983	45	45.3 (72)	1943 (76)	Until 2004/2005

159 *Determination of complete deglaciation is based on an interpolation between the two glacier outlines within which the sites have become ice-free
160 by calculating the euclidean distance as proposed by Betz-Nutz et al. (2023).



161

162 **Figure 1: Location of the sites, glacier outlines (Sources in Table 2) and location for meteorological data extraction (for**
 163 **corresponding analysis, see sec. 3.3).** Large-scale elevation data (DSM, 25 m) (centre right) are based on SRTM and ASTER GDEM
 164 (Copernicus, 2016). DEMs (1 m) (right and bottom right) are based on airborne LiDAR (ALS) data from 2017 (Kaunertal) and 2019
 165 (Horlachtal and Martelltal) (see sect. 3.1.1). Orthophotos (from 2020) are provided by the Province of Tyrol (Horlachtal and

166 Kaunertal) and by the Autonomous Province of Bolzano, South Tyrol (Martelltal). The glacier outline of Groß and Patzelt (2015) is
 167 based on mapping of the LIA lateral moraines and field surveys based on orthophotos. In the process of this study, these mappings
 168 were slightly modified so that they fit to the maximum glacier outline (LIA lateral moraines) more accurately. The glacier outlines
 169 end of LIA, 1918, 1945 and 1959 in the Martelltal have already been described by Betz et al. (2019).

170 **Table 2: Sources of the glacier outlines.**

Valley	Year	Source
Horlachtal	End of LIA	Groß and Patzelt (2015)
	1889	Gedächtnisspeicher Ötztal (Austria, Längenfeld), K&K Militärgeographisches Institutsarchiv*
Kaunertal	End of LIA	Groß and Patzelt (2015)
	1886/1887	Finsterwalder and Schunck (1888)*
	1922	Finsterwalder (1928)*
	1953	Images of BEV, DoD 1953/2017***
	1970/1971	Images of the Office of the Tyrolean Government, DoD 1970/1971-2017***
	2006	Province of Tyrol, DoD 2006-2017***
	2017	Chair of Physical Geography, Cath. University Eichstätt-Ingolstadt, SEHAG-project (See sect. 3) **
Martelltal	End of LIA	Mapped on base of visible moraines and descriptions of Finsterwalder (1890)
	1918	Spezialkarte 1:75.000 of BEV*
	1945	Images of the IGMI, orthofoto*
	1959	Images of IGMI, DoD 1959-2019***
	2004/2005	Autonomous Province of Bolzano, DoD 2004/2005-2019***

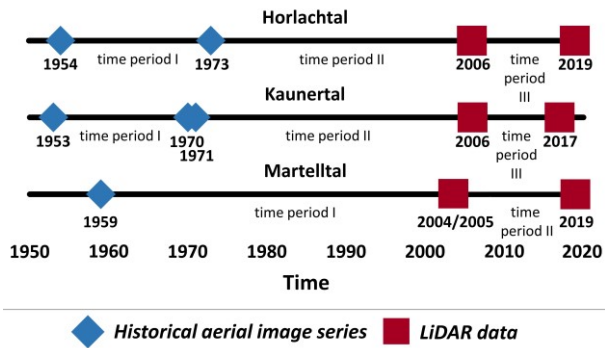
171 *based on historical map, **based on orthophoto and/or hillshade and ***based on DoD (SfM-MVS/photogrammetry and/or ALS).

172 **3 Material and Methods**

173 **3.1 Generation of the topographic data**

174 **3.1.1 Processing of airborne LiDAR and photogrammetric/SfM-MVS point clouds**

175 Several data sets were used for the reconstruction of the terrain surface for the entire catchments. These include both current
 176 airborne LiDAR data and historical aerial image series (Figure 2). Thus, the time periods are based on the availability and
 177 quality of the data.



178

179 **Figure 2: Type of topographic dataset and the resulting time periods.**

180 To determine the recent morphodynamics in the respective sites, available airborne LiDAR data from 2004/2005 to 2019 were
 181 used. The 2004/2005 and 2006 data of the three valleys were provided by the Autonomous Province of Bolzano and the
 182 Province of Tyrol (Table 3). The latest ALS datasets of each valley (2017 and 2019) were collected in own ALS flight
 183 campaigns of the Chair of Physical Geography at the Catholic University of Eichstätt-Ingolstadt (Table 3) (Stark et al., 2022).
 184 In this case, LiDAR data sets were collected using previously determined flight strips. Direct georeferencing (position and
 185 altitude) of the trajectories was determined by Global Navigation Satellite System (GNSS) rover antenna and an Inertial
 186 Measurement Unit (IMU) (Applanix AP 20), both located in the laser scanner. In addition, GNSS correction data were acquired
 187 on the ground during the flight missions using a dGNSS antenna (Figure 3).

188 **Table 3: ALS and DEM data and corresponding flight mission attributes.**

Valley	Date of acquisition	Source/Purpose	Laser-scanner	Field of view (°)	Flying altitude (metre above ground)	Air-speed (kn)	Laser pulse Measuring frequency (khz)	Wave-length (nm)	DEM res. or mean point density of the sites (points/m ²)
Horlachtal	05.09.2006	Province of Tyrol	N/A	N/A	N/A	N/A	N/A	N/A	DEM, 1 m
	08.08.2019	SEHAG project (“SEnsitivity of High Alpine Geosystems to climate change since 1850”)	Mobile laser scanner VPI (Riegl VuxSys-LR)	180	~150	~45	200	1550	24.1
Kaunertal	05.09.2006	Province of Tyrol	N/A	N/A	N/A	N/A	N/A	999	3.4
	05.07.2017	PROSA project (“High-resolution measurements of morphodynamics in rapidly changing PROglacial Systems of the Alps”)	Mobile laser scanner VPI (Riegl VuxSys-LR)	180	~150	~45	200	1550	35.7
Martelltal	2004/2005	Autonomous province of Bolzano	N/A	N/A	N/A	N/A	N/A	N/A	1.4

09.08.2019	SEHAG project ("SEnsitivity of High Alpine Geosystems to climate change since 1850")	Mobile laser scanner VP1 (Riegl VuxSys- LR)	180	~150	~45	200	1550	13.3
------------	--------------------------------------------------------------------------------------------------	------------------------------------------------------------	-----	------	-----	-----	------	------

189



190

191 **Figure 3: ALS data collection on 08.08.2019 in Horlachtal. Helicopter with nose-mounted VP1 laser scanner as well as the ground**
 192 **station which recorded the dGNSS raw data during the flight time (Stonex S9III).**

193 In order to extend the temporal scope of this study by several decades (until 1953), previously digitised (high-resolution)
 194 overlapping historical aerial images were processed into historical DEMs. Except for the 1959 Martelltal-survey, camera
 195 distortion parameters and focal lengths were provided for all data with the respective camera calibration certificates (Table 4).
 196 The digitised image series were processed with the Agisoft Metashape Professional software package (Version 1.6.6; Agisoft
 197 LLC) using Structure from Motion (SfM) photogrammetry with multi-view-stereo (MVS) algorithms to generate high-
 198 resolution point clouds. The generation of point clouds from digitised historical (aerial)image series requires different
 199 preparation and processing steps. First, all images of each series were resized to a common image size (uniform number of
 200 pixels along the x- and y-axis) without changing the image content. This step was necessary so that the software can assign all
 201 images to the same camera (source) and was carried out using Adobe Photoshop (CS6). This is of enormous importance in
 202 order to be able to use the appropriate distortion parameters for the respective camera models for the calculation. After, the
 203 image sets were imported into single folders and a common global coordinate system (ETRS89/UTM zone 32N; EPSG code:
 204 25832) was defined. Next, all images were masked to exclude the black borders/frame (instrument stripes with the camera
 205 metadata) in order to avoid interference with the orientation of the cameras (Gomez et al., 2015). Before the initial processing
 206 of images we defined the fiducial mark information and lens distortion parameters in order to set the metric dimension of
 207 images and lenses. This informations were included and used for the alignment of single images (SfM).

208 Since a global exterior orientation requires a large number of precisely surveyed ground control points (GCPs) distributed
 209 throughout the area, we used highly-precise ALS datasets with millimetre accuracy (2019 Horlachtal; 2017 Kaunertal) to
 210 extract these GCPs and to define the exterior orientation of all data. The selection and extraction of GCPs was based on clearly
 211 identifiable objects (e.g. rock formations) that were also considered as stable (geomorphologically unchanged) over the entire
 212 observation period. If a calibration certificate was available, the film camera option was used, fiducial marks defined, the focal
 213 length set and fixed. All other lens distortion parameters ($C_x, C_y, k_1, k_2, k_3, p_1$ & p_2) were estimated and adjusted fully automatic
 214 using the auto-calibration function. In case of missing camera calibration certificate, an auto-calibration (no film camera) was
 215 performed. Both options were proposed by Stark et al. (2022).

216 According to these pre-processing steps, the point clouds were generated by (i) initial joint orientation of the images, (ii)
 217 selection of ground control points (GCPs), (iii) final camera orientation (bundle block adjustment) including scale definition,
 218 and (iv) calculation of dense point clouds.

219 The processing of the 1959 point cloud, which was used in this study, is already described in Betz et al. (2019).

220 **Table 4: Overview of acquired historical image series for point cloud generation and corresponding DEMs by photogrammetry/SfM.**

	1953 (Kaunertal)	1954 (Horlachtal)	1959 (Martelltal)	1970 (Kaunertal)	1971 (Kaunertal)	1973 (Horlachtal)
Source/ Purpose	BEV/Forest condition estimation; Flight C	BEV/Forest condition estimation; Flight D	IGMI	Office of the Tyrolean Government/ Tyrolean state Surveying flight	Office of the Tyrolean Government/ Tyrolean state Surveying flight	Office of the Tyrolean Government/ Tyrolean state Surveying flight
Date of acquisition	31.08.1953/ 01.09.1953/ 08.09.1953	31.08.1954/ 04.09.1954	09.09.1959/ 20.09.1959	29.09.1970	18.08.1971	06.08.1973
Flying altitude (m a.s.l.)	ca. 5955/ unknown ca. 5850	ca. 6110/ ca. 5920	ca. 5100/ ca. 5000	ca. 8665	ca. 5025	ca. 4900
Camera	Wild RC/5	Wild RC/5	Santoni	Wild RC5/RC8	Wild RC5/RC8	Wild RC5/RC8
Number of images	36/51/63	32/4	2/6	26	31	88
Focal length (mm)	210.11	210.23	153.41	210.43	209.48	210.43
Scanning Resolution (μm)	15	15	N/A	12	12	12
Format	TIFF	TIFF	TIFF	TIFF	TIFF	TIFF
Calibration protocol available	yes	yes	no	yes	yes	yes
Number of GCPs	100	74	23	88	29	67
Mean point density (points/m ²)*	8.5	3.7	4.9	13.3	15.7	20.5

Ground resolution (cm/pix) **	22.5	34.8	19.6	19	17	13.8
RMS reprojection error (pix) **	0.48	0.51	1.55	0.86	0.44	0.45

221 *refers to the exact sites, **refers to the entire data set

222 3.1.2 Digital elevation model (DEM) and DEM of Difference (DoD) processing

223 Although all point clouds were finally available in the same coordinate system (ETRS89/UTM Zone 32N, EPSG Code: 25832), a
224 local adjustment of each site was carried out to obtain the highest possible accuracy of the subsequent DoDs to be calculated.
225 For this purpose, stable areas, i.e. geomorphologically unchanged areas such as rock outcrops or stable areas on the lateral
226 moraines, were mapped next to each site based on orthophotos. To match the point clouds as well as possible, the Iterative
227 Closest Point algorithm (ICP) (Besl and McKay, 1992; Bakker and Lane, 2017) implemented in SAGA-LIS (Conrad et al.,
228 2015) was used for fine registration. Previously, the LiDAR based point clouds were further processed in the software SAGA-
229 LIS (LIS Pro 3D) from Laserdata (laserdata.at) in combination with Python and R to prepare point clouds for the generation
230 of high-resolution digital elevation models (DEMs). This included the removal of outliers (Remove Isolated Points), a ground
231 classification (to remove vegetation), which was carried out with a modified approach according to Hilger (2017) and the
232 achievement of more homogeneous point clouds with the tool 3D Block Thinning (PC) in SAGA-LIS. The point clouds were
233 then converted into DEMs using the Point Cloud to Grid tool in SAGA-LIS (elevations of points averaged for each raster cell;
234 cell sizes for Horlachtal and Kaunertal 1m, for Martelltal 2m). Finally, the DoDs were generated by subtracting the individual
235 DEMs from each other to determine the positive and negative elevation changes of the earth's surface.

236 3.1.3 Data statistics

237 The presence of various uncertainties in differently generated DEMs (Hodgson and Bresnahan, 2004; Bakker and Lane, 2017)
238 also leads to uncertainties in the resulting DoDs (Lane et al., 2003; Rolstad et al., 2009; Cavalli et al., 2017; Anderson, 2019).
239 Therefore, an uncertainty assessment was carried out using the DoD values from stable areas near each site. The size of the
240 stable areas varied between 25% and 75% of the size of the corresponding site. In addition to the estimation of the precision
241 (Std Dev) and accuracy (RMSE), the arithmetic mean, minimum and maximum values were also determined (Figure 4).

246 To determine the uncertainty of the sediment volume change (total sediment output, Figure 7), the error propagation method
247 for uncorrelated, correlated and systematic error according to Anderson (2019) was applied. No threshold has been set for the
248 level of detection of the DoDs, as Anderson (2019) clearly recommends not using this for volumetric calculations as it leads
249 to bias in the results. For the final determination of the total error, the following formula was applied Eq. (1):

$$250 \sigma_v = \sqrt{\sigma_{v,re}^2 + \sigma_{v,sc}^2 + \sigma_{v,sys}^2}, \quad (1)$$

251 where $\sigma_{v,re}$ is the uncorrelated error, $\sigma_{v,sc}$ spatially correlated error and $\sigma_{v,sys}$ systematic error.

252 3.2 Derivation of the regression lines

253 In this study, we followed the sediment contributing area approach of Neugirg et al. (2015a; 2015b; 2016) and Dusik et al.
254 (2019), who applied this approach at the slope scale and replaced real sediment traps in the channels, as originally based on
255 the work of Haas (2008) and Haas et al. (2011) using the *sediment contributing area model*, with so-called virtual sediment
256 traps in modelled channels in a DEM (Fig. 5).

257 The *sediment contributing area model* uses an empirical relationship between log. sediment contributing area as the
258 independent variable and log. mean annual bedload sediment yield as the dependent variable. Thus, the sediment contributing
259 area can be used as a predictor of sediment delivery in alpine catchments.

260 Linear regression analysis was used to show this significant correlation, which is formulated as Eq. (2):

$$261 y = \text{intercept} + \text{slope} * x, \quad (2)$$

262 where y is (log.) mean annual bedload sediment yield and x (log.) sediment contributing area.

263 This has already been confirmed in several studies in both small and large catchments (ranging from hectare to square
264 kilometres) and in different regions such as the Northern Calcareous Alps (Haas, 2008; Haas et al., 2011; Sass et al., 2012;
265 Huber et al., 2015) and the French Northern Alps/Prealps (Altmann et al., 2021). Finally it can be stated that a linear
266 dependency of two variables x and y on a log-log-scale has a fundamentally different behavior than a usual linear dependency.
267 In our case, we have $y = \log(\text{sediment yield})$ and $x = \log(\text{sediment contributing area})$. Back-transformation of Eq. (2)
268 using the *exp* function yields gives the following relation between sediment contributing area and sediment yield, Eq. (3):

$$269 \text{sediment yield} = \exp(\text{intercept}) * \text{sediment contributing area}^{\text{slope}} \quad (3)$$

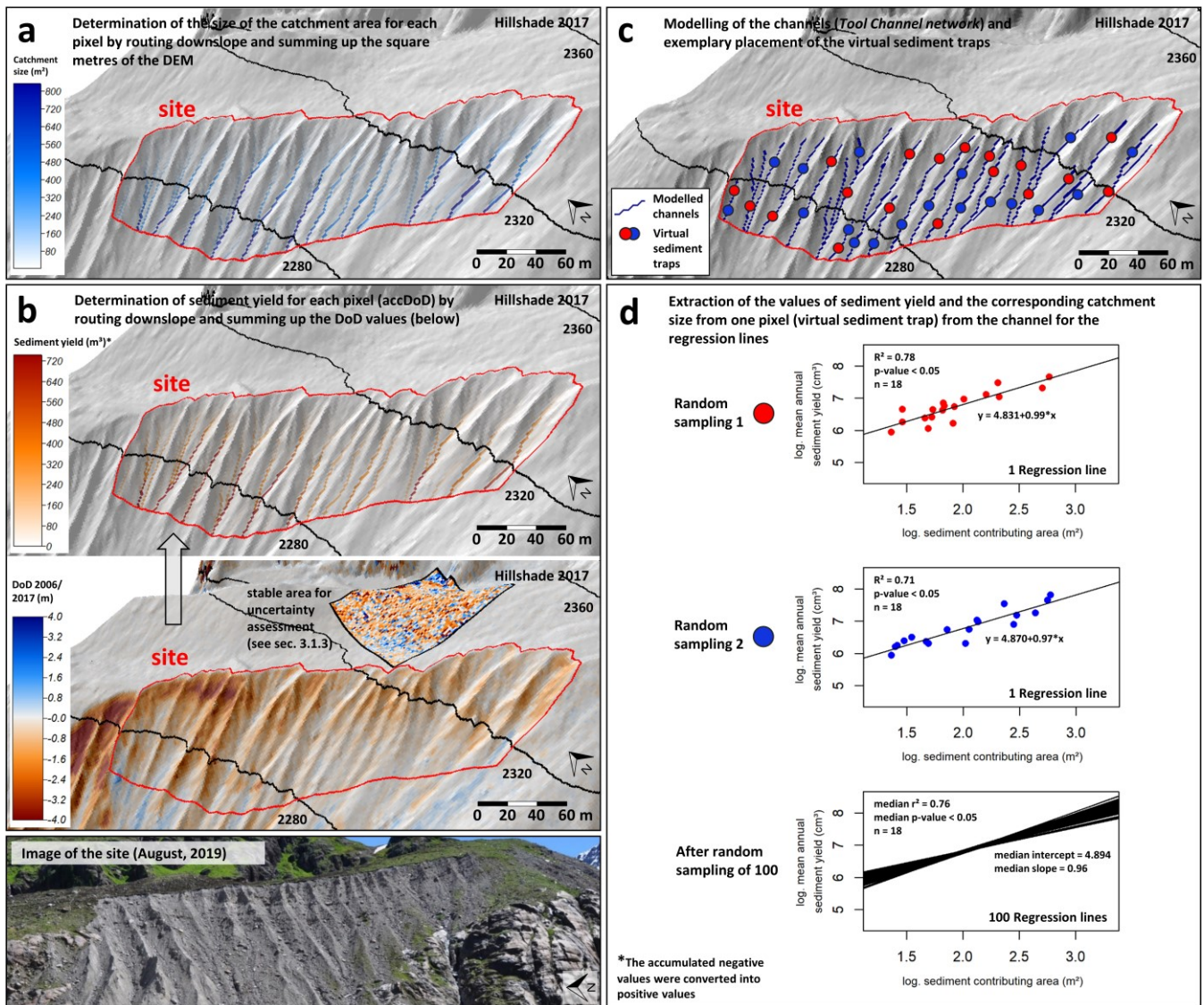
270 Thus, the relation between sediment yield and sediment contributing area is a polynomial of the form $y = a * x^b$. In particular,
271 the slope in the log-log model represents the exponent of the polynomial in the standard model. The relation between sediment
272 yield and sediment contributing area is (nearly) linear if slope is (close to) one. In this case, the exponential of the intercept in
273 the log-log model represents the slope of the linear relation in the standard model, meaning that independent of the actual size
274 of the sediment contributing area, one square meter provides the same amount of sediment yield, given by *exp(intercept)*.
275 On the other hand, if the slope in the log-log model is considerably greater than one, the standard model shows a polynomial

276 behaviour, meaning that in the same site, increasing the sediment contributing area provides more sediment yield per square
277 meter.

278 The steps of the sediment contributing area approach of this study are composed as follows and were implemented in SAGA
279 LIS and R. The elevation changes in DoDs (using no threshold) generated from multitemporal data were routed downslope
280 and accumulated using the D8 algorithm (O'Callaghan and Mark, 1984). The resulting accumulated DoD values (accDoD) in
281 every raster cell corresponds to the net volume of the sediment balance within its contributing area. On steep slopes, accDoD
282 will be negative and represents the sediment yield of this contributing area (Pelletier and Orem, 2014); if it is close to zero, it
283 means that all eroded sediment has been re-deposited within the contributing area. As in the previous sediment contributing
284 area studies by Neugirg et al. (2015a; 2015b; 2016), the application of the parameters used in the original *sediment contributing*
285 *area model* (Haas, 2008; Haas et al., 2011), which lead to the reduction of the hydrological catchment to the sediment
286 contributing area, is omitted because the sites and the modelled channels are consistently steep, uncovered and have short slope
287 lengths, which makes this reduction obsolete. Therefore, the sediment contributing area is identical to the catchment area in
288 this study.

289 In detail, channel initiation points were delineated using a threshold of 20 m² of the flow accumulation that was computed
290 using the D8 algorithm (O'Callaghan and Mark, 1984). Channels that were shorter than 10 m were discarded. To ensure
291 statistical independence through avoiding overlapping contributing areas, a stratified sampling scheme was adopted that
292 included one randomly selected raster cell per channel. Pairs of values (sediment yield and the corresponding sediment
293 contributing area size) were randomly extracted from the corresponding channels for each site and a regression line were
294 calculated accordingly. To quantify the uncertainty due to random selection, this sample was repeated 100 times, resulting in
295 100 regression models of sediment yield on sediment contributing area.

296 Furthermore, we added two conditions and further developed the sediment contributing area approach accordingly. In order to
297 obtain more stable regression lines, the range of values of the sediment contributing area size was divided into quartiles (with
298 equal number of cells within the quartiles) to ensure a homogeneous distribution of the extracted values. Additionally samples
299 that contained points with a high leverage (greater than 0.5) in the regression model were discarded, and the sampling was
300 repeated until a number of 100 samples was reached.



301

302 **Figure 5: Derivation of the sediment contributing area approach using the example of test site KG2: (a) Determination of the size of**
 303 **the catchment area, (b) determination of sediment yield, (c) modelling of the channels and exemplary placement of the virtual**
 304 **sediment traps and (d) calculation of the regression lines.**

305 3.3 Calculation of the sediment output

306 Additionally, the total sediment output volume, the mean annual sediment output (divided by the corresponding number of
 307 years) and the specific mean annual sediment output (additionally divided by the area of the site) were calculated for each site
 308 and time period.

309 The following equation was used for this (4):

$$310 V = \sum D oD * L^2, \quad (4)$$

311 where Σ DoD is the sum of the corresponding DoD subset values and L^2 is the cell size.

312 **3.4 Generation of meteorological data**

313 Using data generated with a regional climate model (RCM), the influence of the changes in climate forcing (air temperature
314 and precipitation) on morphodynamics was investigated. For dynamical downscaling of climate data for the beginning of the
315 study period until 2015, we used the Advanced Research Version of the Weather Research and Forecasting (ARW-WRF)
316 model (version 4.3), which is based on fully compressible and non-hydrostatic equations (Skamarock and Klemp, 2008). The
317 20th Century Reanalysis version 3 (20CRv3) dataset (Compo et al., 2011; Giese et al., 2016; Slivinski et al., 2019), with a
318 spatial and temporal resolution of $1^\circ \times 1^\circ$ and three hours, respectively, was used as driving data (initial and boundary
319 conditions). The simulation was performed in three nested domains with grid spacing of 18- (Domain 1), 6- (Domain 2), and
320 2-km (Domain 3). For our simulations, we mainly used the physics and dynamics options proposed by Collier and Mölg
321 (2020), and are listed in Table 5. However, the Noah land surface model, prescribed eta levels by Collier et al. (2019), and the
322 24 United States Geological Survey (USGS) land use categories were used. The temporal resolution of simulated data in D3
323 is 1 hour for temperature and 15 minutes for precipitation.

324 **Table 5: Overview of the WRF configuration.**

Domain configuration	
Horizontal grid spacing	18-, 6-, 2-km (D1, D2 and D3)
Grid dimensions	190 x 190, 151 x 142, 121 x 139
Lateral boundary condition	variable (20CRv3 at $1^\circ \times 1^\circ$, 3-hour)
Time step	90, 30, 10 s
Vertical levels	50
Model top pressure	10hPa
Model physics	
Microphysics	Morrison (Morrison et al., 2009)
Cumulus	Kain-Fritsch (none in D3) (Kain, 2004)
Radiation	RRTMG (Iacono et al., 2008)
Planetary boundary layer	Yonsei State University (Hong et al., 2006)
Atmospheric surface layer	Monin Obukhov (Jiménez et al., 2012)
Land surface	Noah (Chen and Dudhia, 2001)
Dynamics	
Top boundary conditions	Rayleigh damping
Diffusion	Calculated in physical space

325

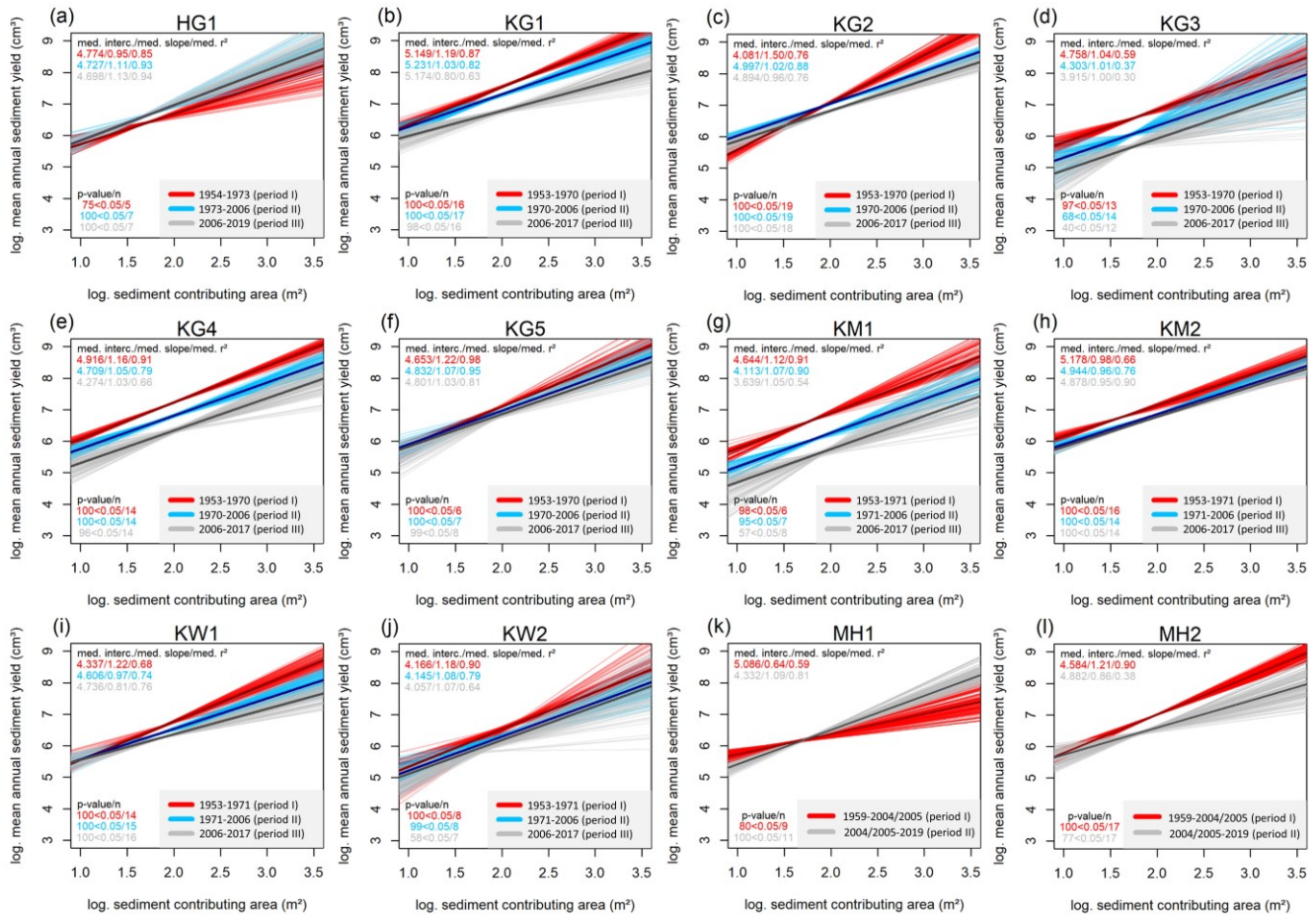
326 The simulated temperature and precipitation data were extracted at the location of each of the five glacier foreland (Figure 1).
327 These are the centres of the respective sites and represent the corresponding glacier foreland. In addition, a corresponding
328 elevation correction of the climate data was applied for temperature.
329 For the analysis, we used the mean annual air temperature (2 metres above ground), as well as the corresponding trends and
330 the mean number of ice days (days with maximum temperature $<0^{\circ}\text{C}$). In addition, the number of warm air inflows from
331 October to May was determined in order to identify corresponding snowmelt processes on the sites. A warm air inflow is
332 defined as a period of at least 2 days in which more than 70% is above 0°C , following a previously colder period of 3 days
333 (100% below 0°C). In addition, the precipitation patterns were analysed. For this purpose, the mean annual precipitation totals,
334 the mean annual winter (October to May) and the mean annual summer precipitation totals (June to September) as well as the
335 corresponding trends were determined in order to identify seasonal changes. Furthermore, various continuing classes (4 mm
336 for one-hour resolution and 10 mm classes for daily totals) were used to analyse corresponding changes in individual extreme
337 events and daily precipitation totals. Individual precipitation events were defined as one event, regardless of length, if they
338 were contiguous throughout, and were separated if there was no precipitation for at least one hour. To minimise the noise
339 generated in the data, both datasets were also filtered for extremely small events by changing the values from <0.01 mm to 0
340 mm. The calculation of the mean annual winter precipitation was always carried out over the entire winter. For example, for
341 the winter of 1953, data from October 1952 to May 1953 was included. The average summer precipitation was calculated
342 accordingly from June 1953 to September 1953. Furthermore, precipitation was differentiated into snow and rain events. The
343 determination of a threshold to distinguish rain from snowfall is very dynamic in mountainous regions and difficult to estimate.
344 However, the difference between rain to snow depends mainly on surface air temperature as well as air humidity, with snow
345 occurring mainly between 0 and 3°C (Froidurot et al., 2014) and the lower the humidity, the higher the probability of snowfall
346 is. In this study, the threshold from rain to snow was defined at $\leq 0^{\circ}\text{C}$, as below this temperature rain is almost excluded
347 (Froidurot et al., 2014; Fehlmann et al., 2018).

348 **4 Results**

349 **4.1 Sediment-Contributing-Area approach**

350 All determined regression lines show a positive correlation between log mean annual sediment yield and log sediment
351 contributing area (Figure 6, Appendix A), which means that sediment yield increases with the corresponding sediment
352 contributing area. In the following, only the median of the 100 regression lines (median slope) of all sites and time periods is
353 used to qualitatively describe corresponding differences. Mostly, there is a decrease in sediment yield between the different
354 time periods and a decrease of the slopes of the regression lines, which is due to a decrease in sediment yield per square metre
355 of the sites. With regard to section 3.3, a decreasing intercept together with an almost constant, although slightly decreasing,
356 slope close to one can be seen over the different time periods in the log-log model, indicating that the relation between sediment
357 contributing area and sediment yield remains almost constant. The sites KG3, KG4, KM1, KM2 and KW2 show such a

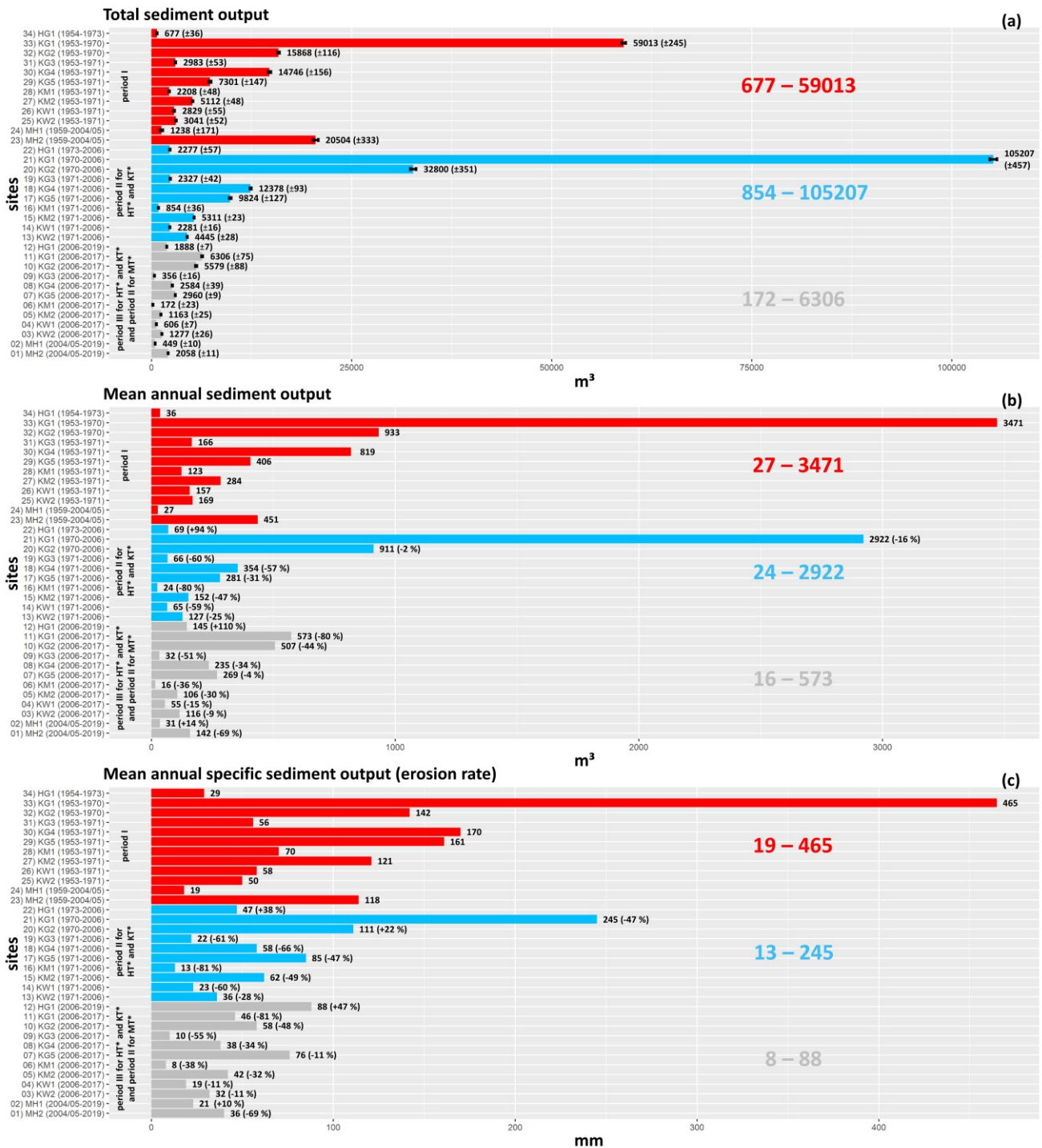
358 behaviour. On the other hand, the areas KG1, KG2, KG5, KW1 and MH2 show clearly larger differences in the time periods.
 359 In the earliest time period, the slopes considerably larger than one (in the log-log model) show polynomial behaviour, which
 360 means that in the same site an increasing sediment contributing area provides clearly more sediment yield per square meter. In
 361 the later time periods, the slopes also tend towards one, so that the models of the different groups become similar. In addition
 362 to this general trend (ten sites), an increase in sediment yield and an increase in the slope of the regression line for site HG1
 363 were observed, showing an increase in sediment dynamics over the time periods in this case, which is in contrast to the previous
 364 observations. Site MH1 shows a similar level of sediment yield (between the time periods) with higher slopes of the regression
 365 lines, also indicating an increase in sediment yield. Furthermore, slopes of the regression lines below 1 occur in all time periods,
 366 but especially in the second and third.



367
 368 **Figure 6: Relationships between log sediment contributing area and log sediment yield yield for 100 samples of each site and the**
 369 **corresponding time periods. In addition, the median regression line (median slope) is represented by a slightly thicker and darker**
 370 **line.**

371 **4.2 Volume calculations of the sediment output**

372 The analyses of the sediment output of the sites confirm the results of the sediment contributing area approach (Figure 7). In
373 general, there is a clear and continuous decrease in mean annual sediment yield of ten sites over the different time periods. In
374 contrast to this trend, site HG1 shows a clear increase in mean annual sediment yield. Site MH1 also shows an increase, but at
375 a very low level, which can also be described as a geomorphic activity of a similar level. In total, the mean annual sediment
376 output decreases across the different time periods. Nevertheless, there is also very high temporal and spatial variability of this
377 change on the sites HG1 and MH1, which also shows a clear increase in geomorphic activity as well as a slight increase
378 (respectively activity at the same level).



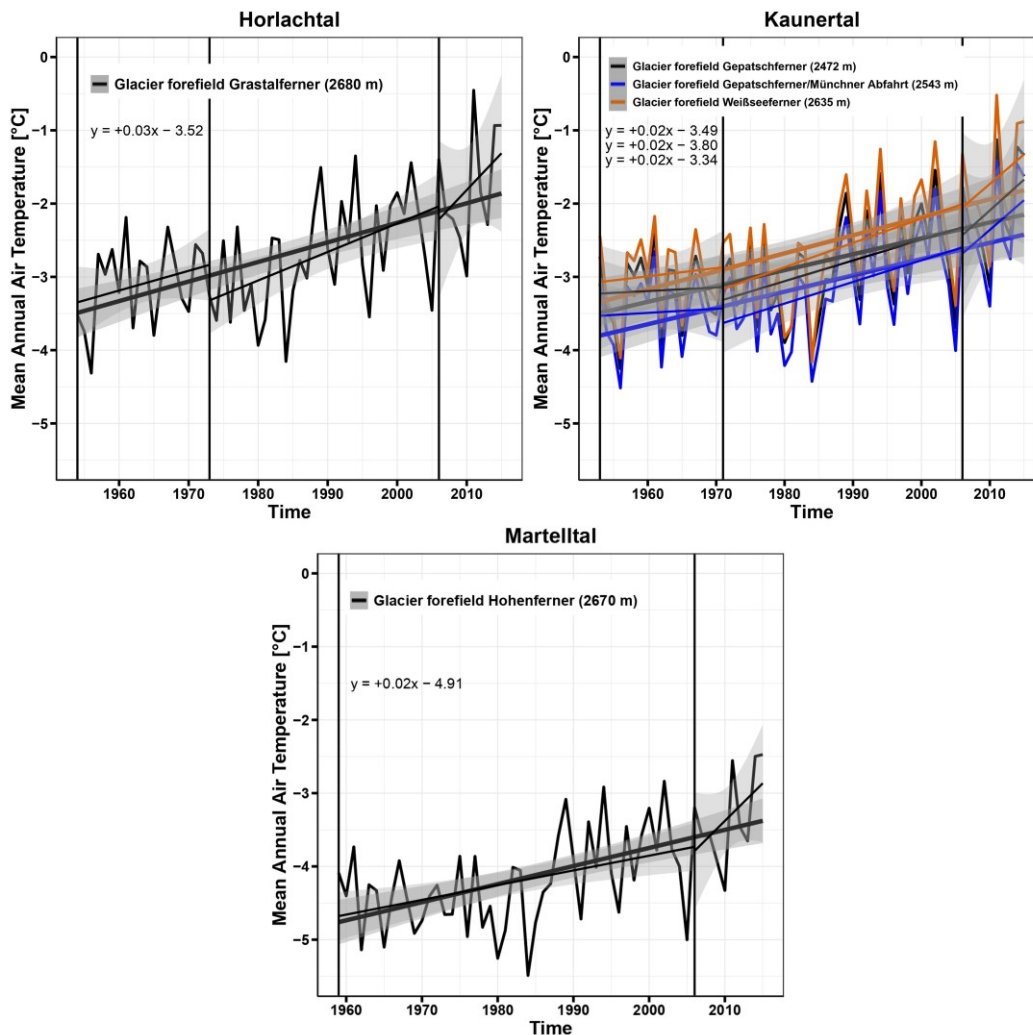
379

380 **Figure 7.** Bar plots of total sediment output (with error range according to Anderson (2019), see sect. 3.1.3 and 3.4), mean annual
381 sediment output and mean annual specific sediment output (erosion rate) of each site and time period.

382 4.2 Meteorological regime

383 4.2.1 Air temperature

384 The mean annual air temperature (2 m above ground) of all selected positions of the glacier forelands shows a statistically
385 significant warming trend over the entire study period of 56, 61 and 62 years (Figure 8). Overall, there is a positive total change
386 of +1.66°C (annual trend +0.03; p-value <0.05; R² 0.35) for the Horlachtal/Grastalferner glacier forelands, +1.36°C (annual
387 trend +0.02; p-value <0.05; R² 0.32) for the Kaunertal/Gepatschferner glacier foreland, +1.74°C (annual trend +0.02; p-value
388 <0.05; R² 0.32) for the Kaunertal/Gepatschferner Münchner Abfahrt glacier foreland, for the Kaunertal Weißseeferner glacier
389 foreland of +1.55°C (annual trend +0.02; p-value <0.05; R² 0.33) and for the Martelltal Hohenferner glacier foreland of
390 +1.41°C (annual trend 0.02; p-value <0.05; R² 0.34).

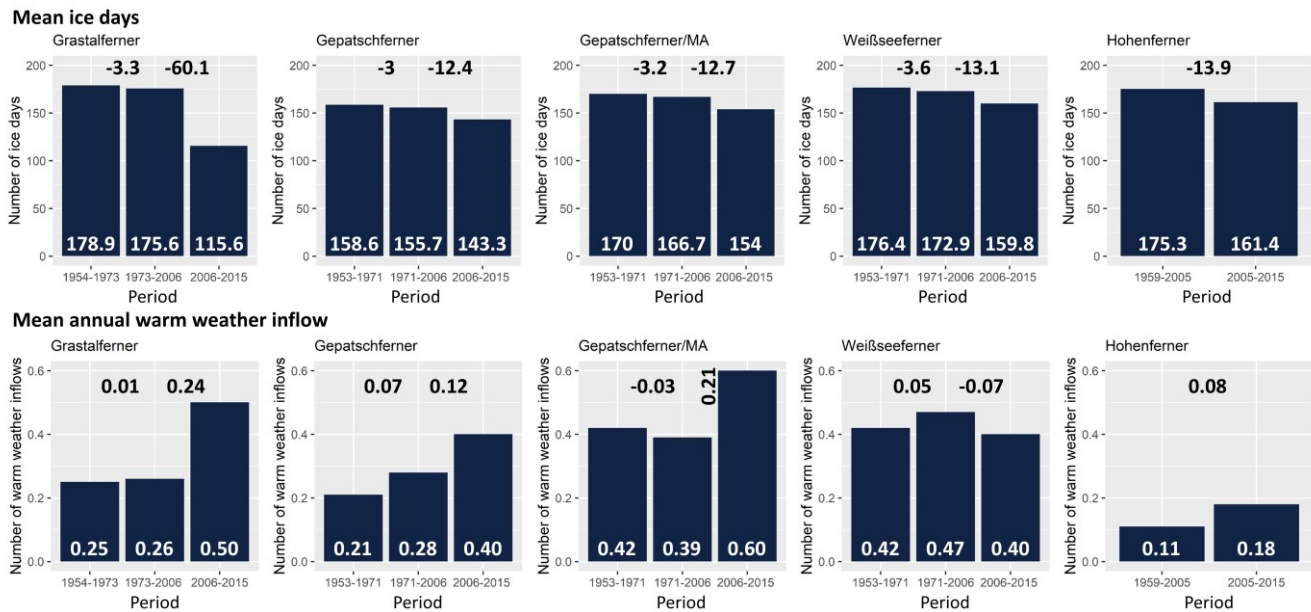


391

392 **Figure 8:** Mean annual 2 meter air temperature of the glacier forelands within the study periods (95% confidence interval is
393 included).

394 The analysis of the mean annual ice days shows a decrease between the time periods, especially from the second to the third
 395 time period (in the Martelltal from the first to the second), with a decrease in ice days between 12.4 and 60.1 days, which
 396 corresponds to almost eight weeks (Figure 9).

397 The analysis of the mean annual warm air inflows shows a general increase of these, especially from the second to the third
 398 period (Grastalferner, Gepatschferner, Hohenferner (first to second period)). In the glacier foreland of the Gepatschferner/MA
 399 the analysis shows a decrease from the first to the second time period, but a more pronounced increase from the second to the
 400 third time period. In the glacier foreland of the Weißseeferner, there is first a slight increase, followed by a slight decrease.



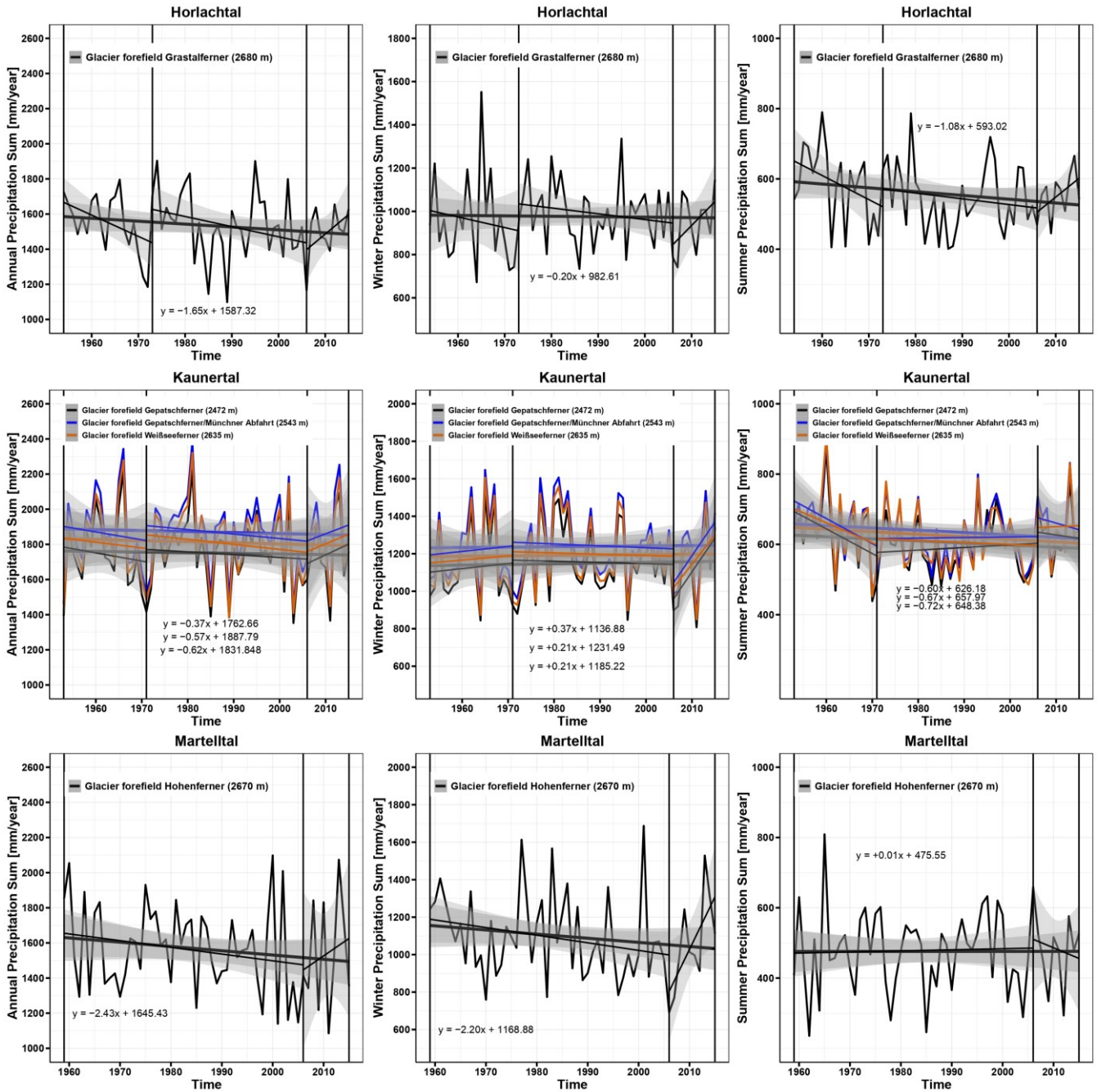
401
 402 **Figure 9: Mean annual ice days and mean annual warm weather inflows with the corresponding changes between time periods.**

403 **4.2.2 Precipitation**

404 Over the entire time periods (56, 61 and 62 years), all study areas show a decreasing trend in mean annual, mean summer and
 405 mean winter precipitation (with the exception of winter precipitation in the Kaunertal and summer precipitation in the
 406 Martelltal, which shows a positive trend) (Figure 10). In the Horlachtal, the first two time periods show a decreasing trend in
 407 precipitation, while the third time period shows an increase in precipitation (mean annual, winter and summer precipitation).

408
 409
 410
 411
 412

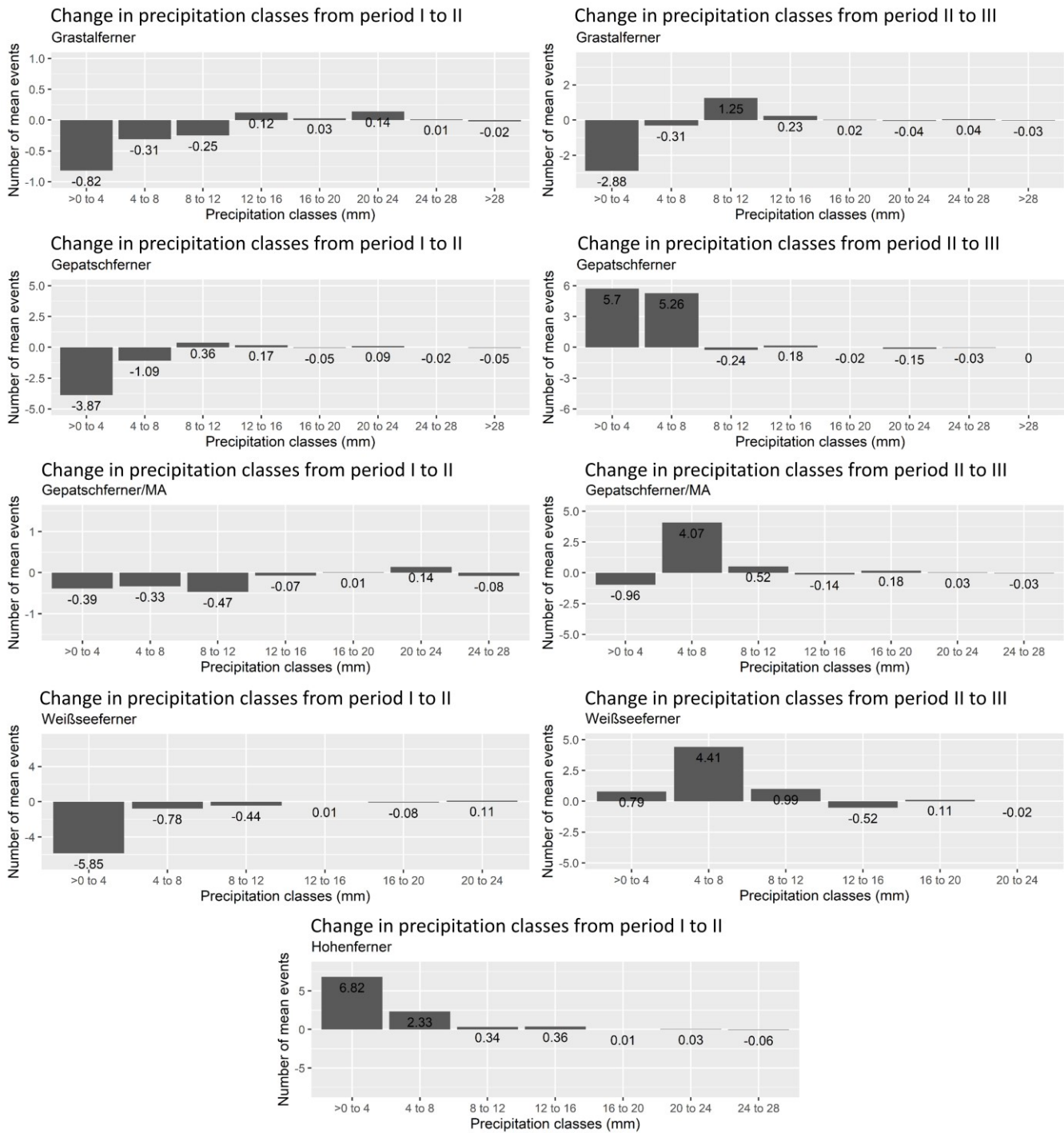
413 In the Kaunertal, winter precipitation shows a slight increase in the first time period and a stronger decrease in summer
 414 precipitation. The second time period shows a slight increase in summer and a slight decrease in winter. The third time period
 415 also shows a strong decrease in summer and an increase in winter precipitation. In the Martelltal, on the other hand, winter
 416 precipitation decreases and summer precipitation increases.



417

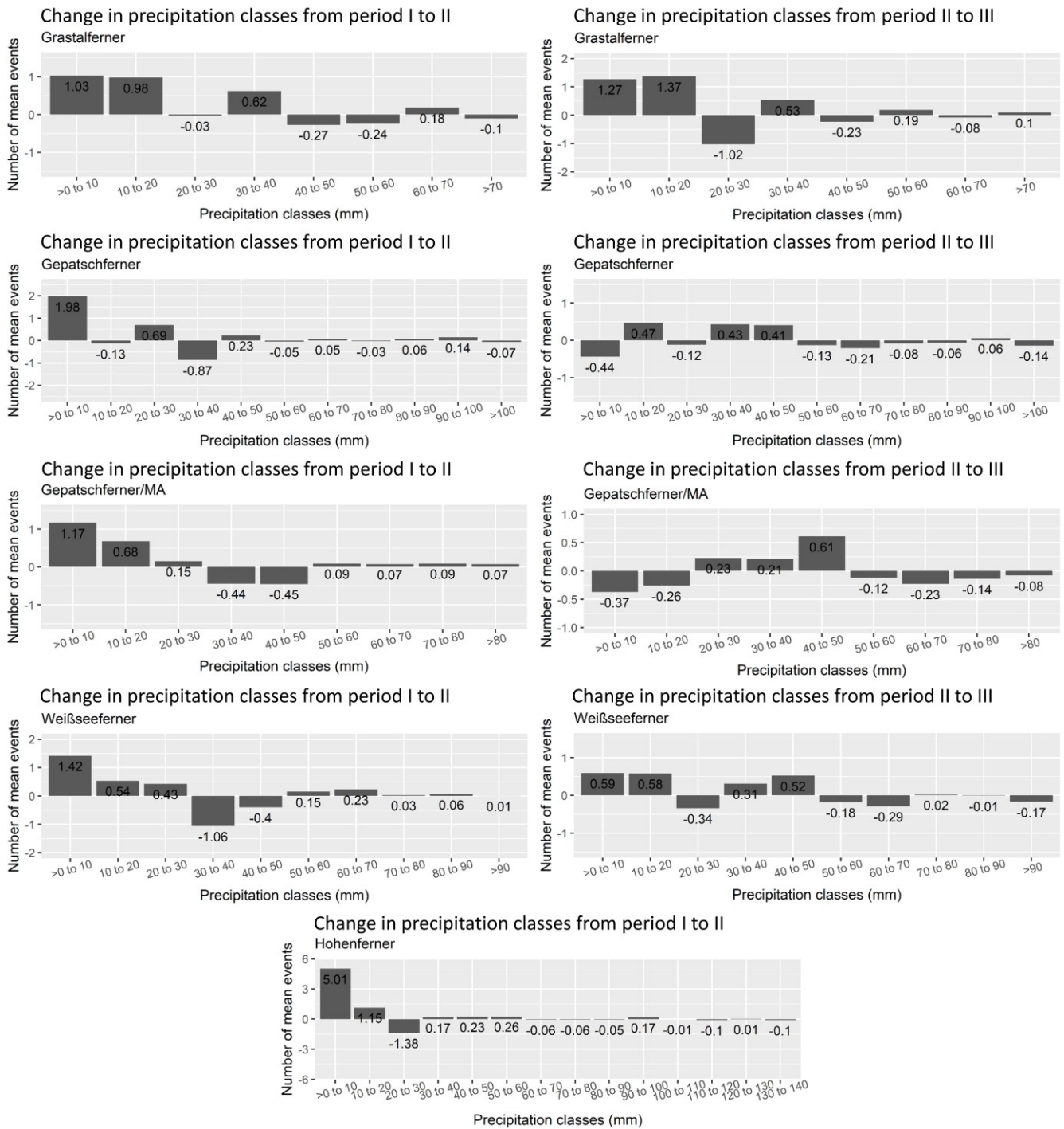
418 **Figure 10: Mean annual, mean summer and mean winter precipitation of the respective glacier forelands.**

419 In the following, the changes of different precipitation classes (as well as with a different temporal resolution) between the
420 individual time periods are analysed. The calculated changes are based on Appendix B and C. In these tables, the number of
421 all precipitation events of the corresponding time periods is shown and divided into corresponding precipitation classes. Using
422 the number of years per time period, this results in an mean annual number of events per class. The calculated changes result
423 from the comparison of the mean occurrence of the precipitation classes of the previous time period. Both precipitation events
424 with a resolution of one hour (Figure 11/Appendix B) and daily precipitation totals (Figure 12/Appendix C) were analysed.
425 The highest temporal resolution (1 hour) shows that the classes >0 to 4 and 4 to 8 are subject to the highest variations (Figure
426 11). In general, it can be seen that the higher precipitation classes tend to decrease, albeit very slightly, but there are still
427 changes with both an increase and a decrease in the different precipitation classes. The daily precipitation totals also show a
428 high variation, with both a decrease and an increase over the different time periods (Figure 12). In general, there are also very
429 slight changes. Nevertheless, the decrease in the higher three classes predominates when comparing the third with the second
430 time period.



431

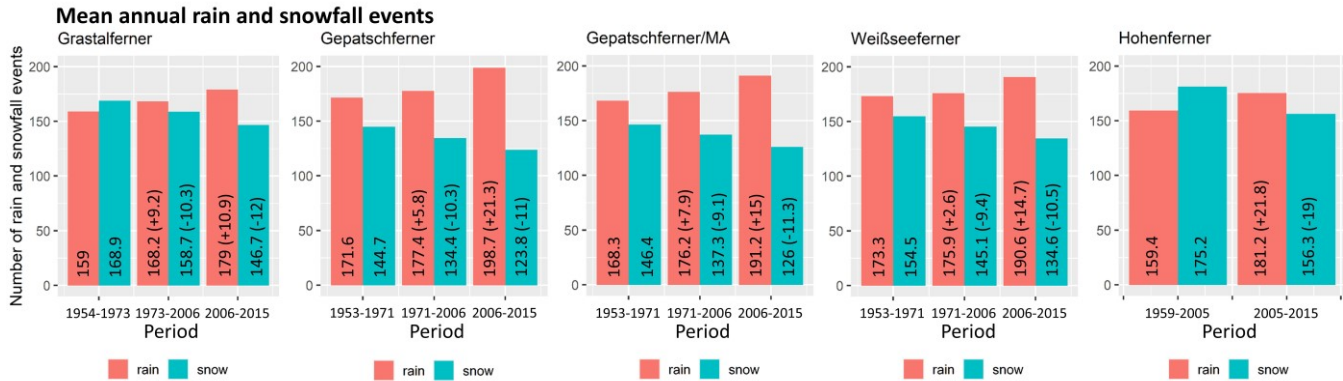
432 **Figure 11: Change in precipitation classes between the different time periods with a one-hour resolution (extreme precipitation**
 433 **events).**



434

435 **Figure 12: Change in precipitation classes between the different time periods with a 24-hour resolution (daily precipitation totals).**

436 The analysis of the mean annual rainfall and snowfall events shows that there is a consistent increase in rainfall and at the
 437 same time a consistent decrease in snowfall (Figure 13).



438

439 **Figure 13: Mean annual rain and snowfall events with the corresponding changes between time periods.**

440 **5 Discussion**

441 **5.1 Assessment of the sediment contributing area approach**

442 Using the relationship between accumulated sediment yield from DoDs and sediment contributing area/catchment area (log-
 443 log model) of different sites and different time periods, we show a long-term monitoring of several geomorphologically active
 444 sections of LIA lateral moraines. This is a clear difference to previous studies that used the space-for-time-substitution (SFTS)
 445 approach in proglacial areas, in which studies used recent morphometrical or morphodynamical differences between sites
 446 located along a gradient of deglaciation age to infer long-term changes in morphodynamics (Ballantyne and Benn, 1994; Curry,
 447 1999; Curry et al., 2006). Means that long-term studies with quantitative data are rare (Schiefer and Gilbert, 2007; Betz et al.,
 448 2019; Altmann et al., 2020; Betz-Nutz, 2021; Betz-Nutz et al., 2023). The approach shown here provides reliable results and
 449 requires only a few input data (Neugirg et al., 2015a; 2015b; 2016; Dusik, 2019; Dusik et al., 2019). The results mainly show
 450 a decrease in sediment yield as well as a decrease in the slope of the regression lines (suggesting less sediment yield per square
 451 metre) over the different time periods, indicating a decrease in geomorphic activity on these sites. In some sites, we observe
 452 contrasting changes: There is an increase in sediment yield and an increase in the slope of the regression line at HG1 and
 453 almost no change in sediment yield on the Y-axis but an increase in the slope of the regression line at MH1, which can be
 454 described as an increase (HG1) and a constant geomorphic activity (MH1). Moreover, in the earlier time periods, a clearly
 455 higher variability of sediment yield (Slope of the regression line clearly higher 1) was observed on the respective sites, which
 456 is no longer reached in the later ones. Thus, it is possible to describe two different types of change in sediment yield (size of
 457 sediment yield between time periods and variability of sediment yield within an time period, which can also be compared with
 458 the other time periods). Slopes of the regression line below 1 could occur when spots appear within the area that are no longer
 459 active, which could be an indication of stabilisation, which occurs mainly in the second and third time period.

460 The p-values of the coefficients are mostly below the alpha level of 0.05, so it is assumed that the relationships between
461 sediment contributing area and sediment yield are statistically significant in almost all cases (~92%) (Figure 6). To determine
462 the proportion of the variance of the dependent variable that can be explained by the independent variable, the R-squares (R^2
463 or the coefficient of determination) of all regression lines were analysed (Figure 6, Appendix A). The relationship between
464 sediment contributing area and sediment yield shows varying correlations within the site and the time periods. The median R^2
465 values range from 0.59 to 0.91 in the first time period, from 0.37 to 0.93 in the second time period and from 0.3 to 0.94 in the
466 third time period (Figure 6, Appendix A). The number of channels modelled differed between the time periods on the same
467 sites due to the different quality of the DEMs and the slightly different size of these. As in Heckmann and Vericat (2018), the
468 accumulation of DoD values resulted in very small positive values at some sites. Such errors are due to the quality of the DoD,
469 different bulk densities of eroded vs. deposited materials, and the inability of the flow routing algorithm to fully reproduce
470 sediment transfer in reality especially when flow directions changed within one time period. Where positive accDoD values
471 occurred, they were small and manually corrected to the zero.

472 Nevertheless, the D8 algorithm simplifies complex sediment transport processes such as fluvial activity, landslides and debris
473 flows, which have different frequencies, magnitudes and forms of erosion and accumulation. As the individual time periods
474 cover several years, no reference can be made in this study to individual processes that can be attributed to extreme precipitation
475 events or to seasonal differences. Therefore, we compare different time periods based on mean annual sediment yield, which
476 includes all geomorphological processes. Accordingly, the aim was not to model individual erosion processes but to compute
477 sediment yield of each cell. The individual sites have a slightly different area within the different time periods, which is mainly
478 due to headcut retreat (Heckmann and Vericat, 2018; Betz-Nutz et al., 2023). The lateral boundaries also changed slightly due
479 to the quality of the DEMs and geomorphological slope processes, while the lower boundary did not change.

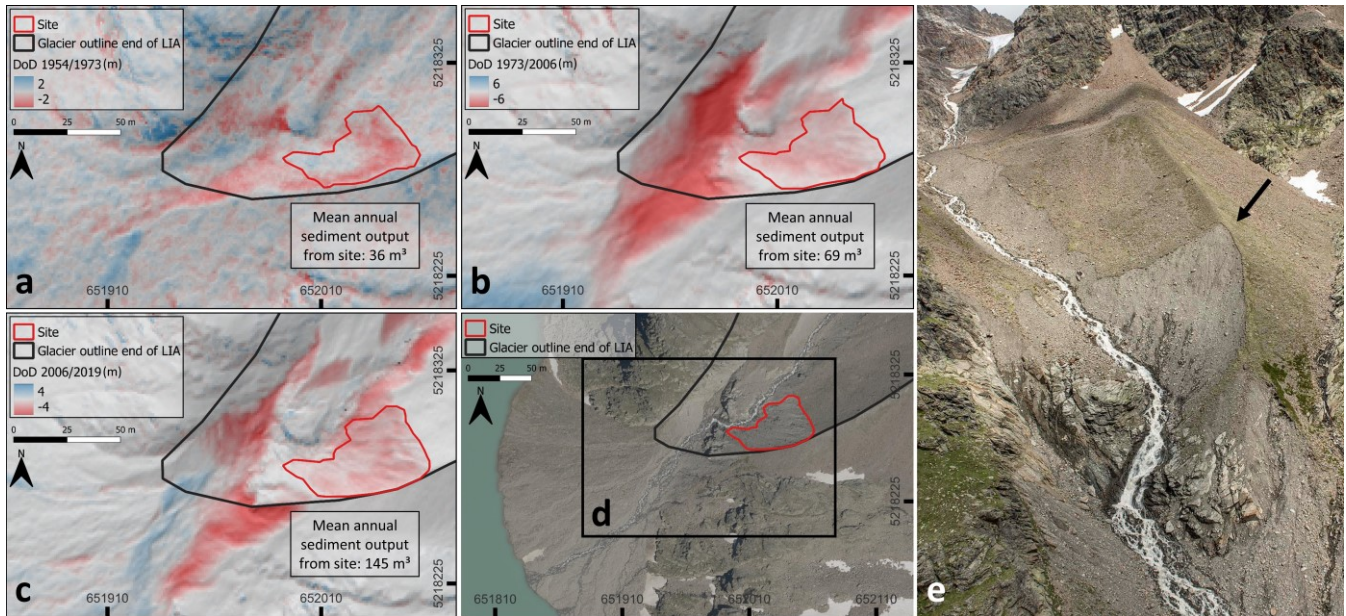
480 By processing historical aerial photographs into DEMs (by SfM-MVS), the temporal aspect of sediment contributing area
481 studies could be quickly and cost-effectively extended to several decades (up to the 1950s), which previously spanned only a
482 few months or several years (Neugirg et al., 2015a; 2015b; 2016; Dusik, 2019; Dusik et al., 2019). However, as Schiefer and
483 Gilbert (2007) have already shown, the shorter the time intervals and the lower the quality of the aerial images, the more
484 difficult it becomes to detect surface changes, so in the process of this study several series of aerial images had to be sorted
485 out that were actually available due to a poor data quality. Furthermore, it should be noted that the accuracy and precision of
486 the historical DEMs strongly depends on the respective generation, e.g. whether they were generated with or without a
487 calibration certificate (as was the case, for example, with the 1959 aerial photo series in the Horlachtal/glacier foreland
488 Hohenferner), which ultimately influences the sediment contributing area results and the calculated erosion rates (Stark et al.,
489 2022).

490 **5.2 Geomorphic activity**

491 The geomorphic activity is directly related to the characteristics of the sites. The sites with the highest mean annual sediment
492 output ($>100\text{m}^3/\text{a}$) (such as KG1, KG2, KG4, KG5, MH2, KM2, KW2) show strong gully formation and are overall

493 characterised by larger areas, longer max. slope lengths and higher mean and max. slope gradients (Table 1). In contrast, the
494 sites with lower mean annual sediment output ($<100\text{m}^3/\text{a}$) (such as KW1, KG3, HG1, KM1, MH1) show less gully incision.
495 These sites tend to be characterised by smaller areas, smaller max. slope lengths and smaller mean slope and max. slope
496 gradients (Table 1). The strong influence of slope length and slope gradient on morphodynamics is also shown by previous
497 studies (Ballantyne and Benn, 1994; Curry, 1999; Curry et al., 2006; Betz-Nutz et al., 2023). KG3 also appears to be somehow
498 stabilized by bedrock in the lower part of the slope, which could mitigate the erosion of this site, as also shown by Jäger and
499 Winkler (2012). Elevation and aspect, however, do not seem to have an influence on geomorphic activity, which is also shown
500 in the study by Curry et al. (2006). Since only bare and sparsely vegetated areas were investigated, no findings on the influence
501 of vegetation on morphodynamics can be made in this study. Solifluction processes could also not be observed, probably due
502 to the composition of the moraine material. Presumably, the morphodynamics are still so high that the vegetation does not yet
503 have the opportunity to develop accordingly. In general, we assume that debris flows are the most common process, as
504 described for example by Ballantyne (2002a) and Curry et al. (2006). Thus, material stored in the gullies is transported
505 downslope by debris flows mainly rain or snow events in the spring or heavy rainfall events during rainstorms in the summer
506 months (Ballantyne and Benn, 1994; Ballantyne, 2002b; Curry et al., 2006; Dusik et al., 2019).
507 However, the high mean annual sediment yield and corresponding erosion rate in the first ($3471\text{ m}^3/\text{a}$, $465\text{ mm}/\text{a}$) and second
508 ($2922\text{ m}^3/\text{a}$, $245\text{ mm}/\text{a}$) time periods of site KG1 (Figure 7) can probably also be attributed to individual landslides and deep-
509 seated slope failures in some cases linked with melting dead ice bodies, as these processes are more likely to occur after
510 deglaciation, and are characterised by high magnitude and low frequency, which has also been shown by Blair (1994),
511 Hugenholtz et al. (2008) and Cody et al. (2020). On the less incised slopes (e.g. MH1), small-scale processes such as fluvial
512 erosion or snow drifts probably occur (Betz-Nutz, 2021), which ultimately show no clear trend in the increase or decrease of
513 morphodynamics, but can be described as a constant geomorphic activity. In Betz-Nutz et al. (2023) and in this study, six
514 similar lateral moraine sections (although other exactly defined sites) were investigated. The test sites KG1, KG2, KW1, KW2
515 and MH1 (in Betz-Nutz et al. (2023): GPF1, GPF2, WSF1, WSF2 and HF1) showed similar erosion rates and the same log-
516 term trends. In the case of site MH2, different trends were determined (stagnation in Betz-Nutz et al. (2023) and a decrease in
517 this study), which can be attributed to the differently defined site and the slightly different study period.
518 In the sense of a process-response system, it is noticeable that the first-mentioned group of sites with the higher erosion rates
519 (except KG1) had considerable influence from melting dead ice in the lower slope area at least until 2006 (KG2, KM2, KW2,
520 MH2) or the glacier was still present at the bottom of the slope (KG4, KG5), which could be identified by the interpretation of
521 the DoDs. Melting of the dead ice can lead to destabilisation of the slope, which can enhance erosion processes of the upper
522 slope areas, as the support is no longer present, the sediment becomes saturated and there can be an increase in the slope
523 gradient due to the subsidence of the lower part of the slope (Altmann et al., 2020; Betz-Nutz et al., 2023). However, the
524 highest slope gradients are also present here, which also plays a major role. In addition, site HG1, where erosion is increasing,
525 shows an undercutting of the slope by the adjacent stream, which leads to a destabilization or lowering of the erosion base and
526 a typical formation of a debris cone and alluvial fan with a successive reduction of the slope gradient is missing (Figure 14).

527 It can be assumed that individual strong rainfall events in the second and third time periods in combination with changing flow
528 paths due to the retreat of the Grastalferner acted here as an impulse and affected both the site itself and the adjacent stream.



529
530 **Figure 14: Overview of the DoDs of the corresponding time periods of site HG1: (a) DoD 1954/1973, (b) DoD 1973/2006, (c) DoD**
531 **2006/2019, (d) Orthofoto 2020 (provided by the Province of Tyrol) and (e) photo of the site from 2019 by Anton Brandl.**

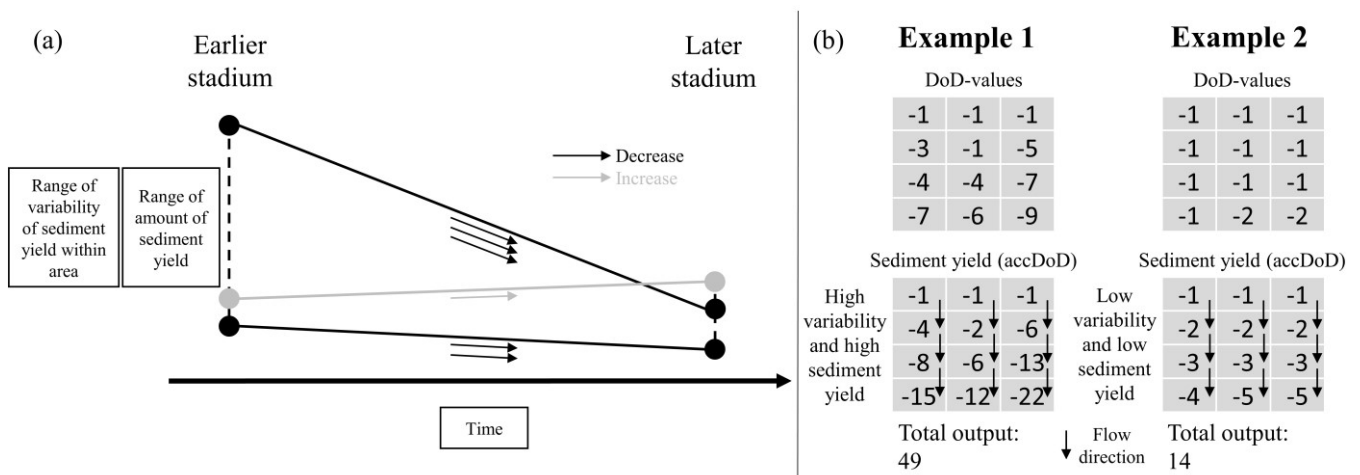
532 5.3 Paraglacial landscape adjustment

533 5.3.1 The "Sediment activity concept"

534 The finding of mainly decreasing geomorphic activity of LIA lateral moraines in this study is largely consistent with previous
535 model-based studies describing the paraglacial landscape adjustment with a decrease in geomorphic activity in proglacial areas
536 over time, such as the theoretical model "paraglacial concept" of Church and Ryder (1972) or the "sediment exhaustion model"
537 of Ballantyne (2002a, 2002b). The geomorphic activity of gully systems is given as a few decades to centuries (Ballantyne,
538 2002a; 2002b). Furthermore, it is stated that there is a high temporal and spatial variability in this development. The model
539 provides an appropriate approximation (Ballantyne, 2002a; 2002b). Within the paraglacial adjustment process, different
540 geomorphological processes result in different durations of occurrence. Furthermore, different land systems react at different
541 rates and on different spatial scales. Thus, external perturbations can occur, leading to secondary peaks and time delays
542 (Ballantyne, 2002a; 2002b). While ten out of twelve sites fit the model descriptions, two test plots show opposite
543 morphodynamics, which can be described as a delay of the paraglacial adjustment process or that response systems can run
544 counter to such an adaption.

545 To estimate the changing morphodynamics, we therefore propose the following simplified description of the landscape
546 evolution using the "Sediment activity concept" based on the results of this study. Due to the study design, this concept is only

547 valid on geomorphologically active areas (in this case the upper lateral moraine section) on LIA lateral moraines and until
 548 about 170 years after the end of LIA (Table 6, Figure 15). The concept distinguishes between an earlier and a later phase. The
 549 earlier phase (mainly 1950s to 1970s) is characterised by a wide range between areas with high and low variability of sediment
 550 yield within the area as well as high and low mean annual sediment yield (erosion rate/volume). In contrast, the later stadium
 551 (mainly 1970s to 2000s and 2000s to the end of the survey 2017/2019) shows a decrease in this range. Although the decrease
 552 of morphodynamics predominates, there are also increases in morphodynamics. The time of ice release was not integrated
 553 here, so that the time periods refer to the actual time. In addition, we give two examples in Figure 15. While example A shows
 554 high variability (polynomial behaviour) within the area and high sediment yield (erosion rates/sediment output), example B
 555 shows low variability (constant/linear behaviour) and low sediment yield (erosion rates/sediment output). Ultimately, the
 556 relationship between sediment yield and the size of the catchment has changed so that erosion within the area is more constant
 557 today.



558
 559 **Figure 15: The "Sediment activity concept". Description and illustration of the change in sediment activity over time (a) and 2**
 560 **corresponding examples (b).**

561 **Table 6: Tabular summary of the simplified conceptual model.**

	Earlier stadium	Later stadium
Sediment yield within area	Highly variable up to constant	In the range of constant
Amount of sediment yield	Wide range	Lower range
Over time	Mostly decreasing	

562
 563 Introducing the "Sediment activity concept" of this study, we present a different description of the paraglacial adjustment
 564 process which is based on the actual sediment yield. However, the concept is only valid until about 170 years after the end of
 565 LIA and on the sites of this study. The "Sediment activity concept" presented here is also compatible with the results of other
 566 studies, as for example Betz-Nutz et al. (2023) mostly show a decrease in erosion rates over a similar time period, but also a

567 remaining at similar levels and an increase. In addition, the studies by Church and Ryder (1972), Ballantyne and Benn (1996),
 568 Curry (1999), Ballantyne (2002a), Curry et al. (2006) and Schiefer and Gilbert (2007) show a decrease in geomorphic activity
 569 over time, which is also consistent with the model presented here. Also, we assume that the concept can also prove its validity
 570 in further proglacial active areas and partly over an even longer period of time.

571 5.3.2 Erosion rates

572 The methodologies for determining long-term average erosion rates in proglacial areas are based on gully volume estimates
 573 (Ballantyne and Benn, 1994; Curry, 1999; Curry et al., 2006) and sediment volume calculations due to surface changes using
 574 DoDs, as shown by Betz-Nutz et al. (2023) and this study (Table 7). In glacier forelands in western Norway, this amounts e.g.
 575 to minimum estimates of 50-100 mm/year (max. estimates of min. 200 mm/year) (Ballantyne and Benn, 1994) and a minimum
 576 of 5.5-169 mm/year (in different glacier forelands) (Curry, 1999). A further study in the Swiss Alps shows erosion rates of
 577 min. 49-151 (in different glacier forelands) (Curry et al., 2006). The work of Betz-Nutz et al. (2023) and this study show
 578 erosion rates over several decades and distinguish between different time periods, which makes it possible to show differences
 579 between them. Both studies show that the mean erosion rates in the individual time periods decrease (Table 7), although in
 580 individual cases there is also a constant and an increase in erosion rates over time. Although there has been a clear decrease in
 581 geomorphic activity, stabilisation of the sites is not yet apparent, which means that the paraglacial adjustment is still ongoing.
 582 Within this study, we observed that the sites still show a high geomorphic activity even after they have been deglaciated for
 583 76-159 years. A stabilisation of the gully systems as shown by Curry (2006) cannot be observed. Other studies such as Lane
 584 et al. (2017), Dusik (2019), Altmann et al. (2020), Betz-Nutz et al. (2023) also show the still ongoing paraglacial adjustment
 585 processes. Comparing the long-term erosion rates of gully systems from the different studies ultimately shows high variability
 586 in the adjustment; as these studies were also conducted using different methods, on different time scales, and in different
 587 regions. Differences are probably mainly due to the different local conditions, such as the geomorphological settings, e.g. the
 588 different characteristics of the lateral moraine sections, such as slope gradient, slope length, time of ice exposure, dead ice
 589 influence and the development of vegetation. Furthermore, the lateral moraines have different sedimentological characteristics
 590 related to their genetic origin. In addition, different meteorological conditions prevail in the different regions.

591 **Table 7: Studies on long-term erosion rates (several decades) of gully systems on LIA lateral moraines in different glacier forelands.**

Study	Erosion rate (mm/year)	Timescale (year)	Time since ice exposure (year)	Location of the study area
Ballantyne and Benn (1994)	Min. of 50-100, max. min. of 200	48	48	Norway, Fåbergstølsbreen
Curry (1999)	Min. of 5.5-8.8, 38- 169 and 19-169	76, 53, 43	76, 53, 43	Norway,

Curry et al. (2006)	Min. of 86-151 and 49-103	55, 79	55, 79	Fåbergstølsbreen, Lodalsbreen and Heillstugubreen Switzerland, Glacier du Mont Miné and Feegletscher
Betz-Nutz (2021; 2023)	Period I: 2-429, period II: 1-186, period III: 3-110	Period I: Mainly ~1950s to ~1970s, period II: ~1970s to ~2000s and period III: ~2000s to 2018/2019	59-154	Austria (Tyrol), Germany (Bavaria) and Italy (South Tyrol), ten different glacier forelands
This study	Period I: 19-465, period II (HT and KT): 13-245, period II (MT) and period III (HT and KT): 8-88	Period I: 17-19 (in HT and KT) and 45/46 (in MT), period II: 33-36 (in HT and KT) and 14/15 (in MT) and period III: 11-13 (in HT and KT)	76-159	Austria (Tyrol) and Italy (South Tyrol), five different glacier forelands

592 *HT = Horlachtal, KT = Kaunertal and MT = Martelltal.

593 5.4 Meteorological drivers

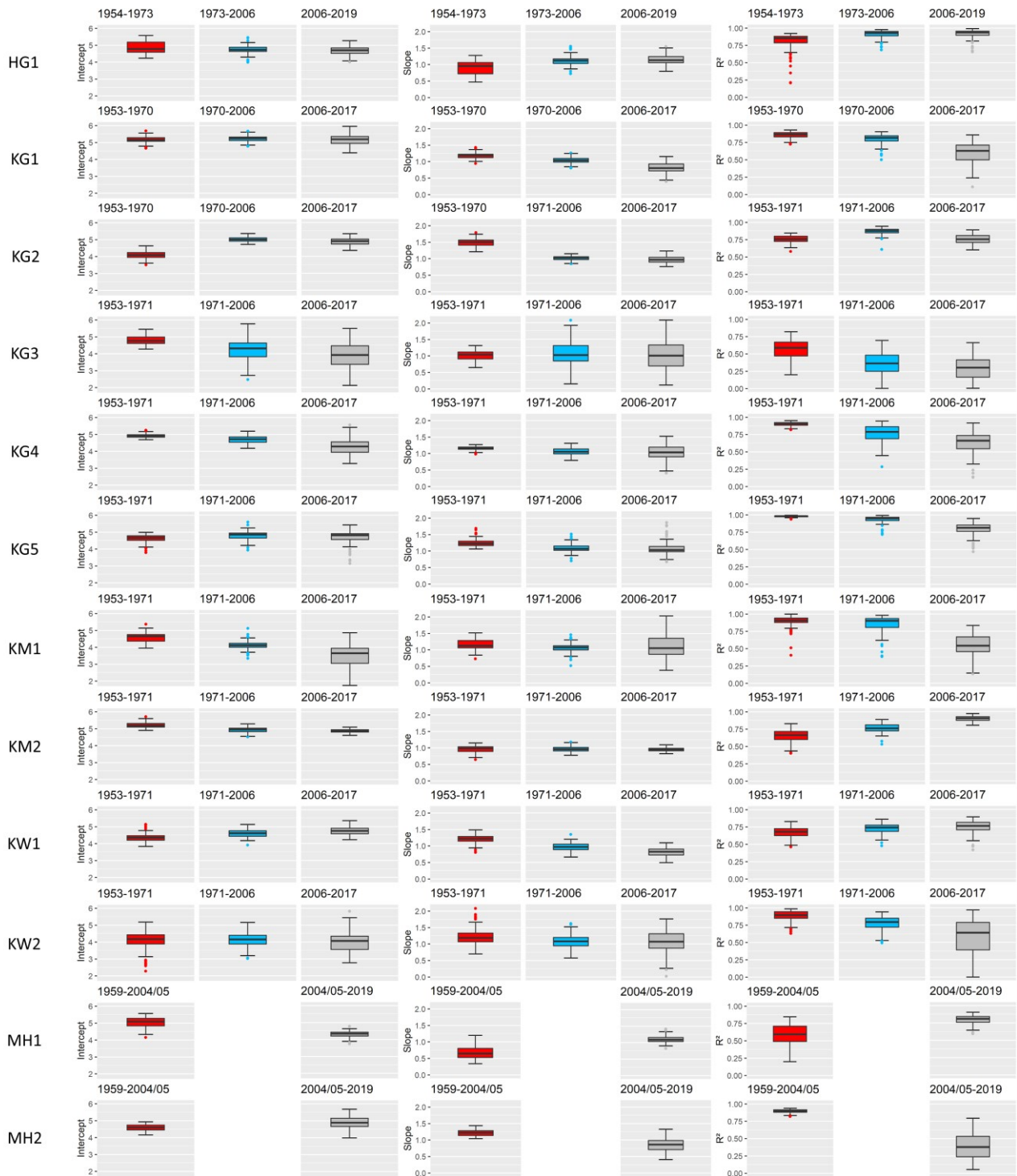
594 The decrease of the mean annual number of ice days and the increase in the number of warm spells over the different time
595 periods and the associated potential increase in snowmelt on the slopes could also lead to an increase in morphodynamics, as
596 these processes represent important preparatory steps for erosion processes in spring (Haas, 2008), such as increased saturation
597 of the slope due to snow melt, loosening of the upper sediment layers or the delivery of material by snow slides or small wet
598 avalanches that is then available for debris flows in the summer months (Dusik et al., 2019). Klein et al. (2016), for example,
599 also show an increase in the frequency and intensity of snowmelt in the Swiss Alps. Mean annual precipitation decreases
600 slightly across time periods, but is not statistically significant (except for winter precipitation for the entire study period (1959
601 to 2019) and summer precipitation in the second time period from 2005 to 2019 in the Martelltal). Other studies also show that
602 the decrease in precipitation in the European Alps is low (Brugnara et al., 2012) and that there is no clear trend in precipitation
603 (Hock et al., 2019) or that it is mainly subject to regional influences and decadal variations (Mankin and Duffenbaugh, 2015).
604 Extreme precipitation events (1h resolution) and daily precipitation totals also show only minor changes. Differentiation of
605 precipitation, on the other hand, shows a clear increase in rainfall and a decrease in snowfall, which is also shown by Serquet
606 et al. (2011), Beniston et al. (2018) and Hock et al. (2019) who found that the rainfall on snow events in spring as preparatory
607 factor for the erosion processes in the summer months increase. The simulated meteorological data generally show lower
608 temperatures and larger precipitation amounts, when compared to three automatic weather stations operated by TIWAG
609 (Tyrolean Hydropower AG, Innsbruck, Austria). These stations are located in the vicinity of our sites. The simulated mean

610 annual temperatures extracted at the location of the weather stations Horlachalm (1987-2015) (approx. 6.5 km linear distance
611 to the site in the Grastalferner glacier forfield) and Weißseeferner (2007-2015) (approx. 500 m linear distance to the sites in
612 the Weißseeferner glacier forfield), covering the same time period indicate a difference of -1.05°C and of -0.87°C , respectively,
613 after accounting for differences in elevation. However, at Gepatschalm (2010-2015) weather station (approx. 2.5 km linear
614 distance to the sites in the Gepatschferner glacier forfield), the difference between the simulated and observed mean annual
615 temperatures is 0.13°C , indicating that the magnitude of the discrepancies depends on the station data used for the comparison.
616 The simulated precipitation, however, is generally larger with mean annual precipitation sums of 1531, 1655, and 1820 mm at
617 the location of Horlachalm (1990-2015), Gepatschalm (2010-2015), and Weißseeferner (2007-2015), respectively, while the
618 weather stations recorded values of 803, 1086, and 924 mm, indicating large discrepancies especially when compared to
619 Horlachalm and Weißseeferner weather stations. The datasets from which the temperature and precipitation were extracted are
620 both based on coarsely resolved data, which makes a comparison with measurement data in the field difficult, although the
621 corresponding trends are well usable for this study. The large difference between simulated and recorded precipitation is mainly
622 due to winter precipitation (Figure 11) when the weather stations are not always able to record total snowfall accurately;
623 additionally, fog precipitation or precipitation in combination with stronger winds are not recorded correctly.
624 The weather and climate study periods are based on the predefined study time periods given by the availability and quality of
625 orthophotos, and not on the usual climate periods. This results in large differences in the length of the different time periods,
626 which must be taken into account.
627 There are several sources of uncertainty in the simulated data, amongst them the dynamic initial and boundary conditions, as
628 the forcing data have their own sources of uncertainties. Furthermore, the choice of the reanalysis data used for forcing the
629 model has an influence on the final results. Additionally, for such long simulations, an updated sea surface temperature (SST)
630 is recommended. Since there are no SSTs available for the 20CRv3, we have generated SST fields from the skin temperature.
631 Other sources of uncertainty are the static boundary conditions like the fixed land use categories and topography, as well as
632 model simplifications and choices in the parameterization of the physics and dynamics. In our simulations, we have used
633 spectral nudging in order to keep the model from large deviations from the forcing data. Short test runs indicate that the use of
634 spectral nudging improves the simulated data, especially with respect to precipitation. However, the strength of nudging also
635 has an influence on the final results. Since the purpose of this study is not to test how strongly to nudge, we have used the
636 default values in WRF.

637 **6 Conclusion**

638 Using DoDs based on SfM photogrammetric and LiDAR data DEMs, we show with two different approaches, the long-term
639 (1953-2019) change in the morphodynamics of several active gully systems on LIA lateral moraines in the Tyrolean and South
640 Tyrolean Alps, Austria and Italy. First, the change in the range of variability of sediment yield within the area (using regression

641 lines with accumulated sediment yield and sediment contributing area/catchment area) and second, the change in the amount
642 of sediment yield (calculation of erosion rates/volume of sediment output) between the different time periods could be shown.
643 Finally, the first time period shows a clearly higher range of variability of sediment yield within the site than the later time
644 periods. This means that the spatial pattern of erosion has become more uniform within the areas. In addition, the total sediment
645 yield, the mean annual sediment yield and the mean annual specific sediment yield (erosion rate) were calculated for each site
646 and time period was calculated. Over the time periods, there is a decreasing trend of geomorphological activity in 10 out of 12
647 sites , while 2 sites show an opposite trend, where morphodynamics increase or remain at the same level. Overall, we confirm
648 the general trend of decreasing morphodynamics over time (10 sites) of several previous studies, although we could also show
649 that the geomorphic activity of one site is on the same level and one is increasing. Finally, the results led to the proposal of a
650 simplified conceptual model “The sediment activity concept”, describing the paraglacial adjustment process by summarising
651 the findings on the long-term morphodynamics of the upper parts (gully heads) of lateral moraines from this study.
652 Despite the general decline in morphodynamics, the sites show no stabilisation, leading us to the conclusion that the paraglacial
653 landscape adjustment is still in progress (even on areas that have been ice-free for at least 159 years). It seems that the
654 vegetation has not yet had the opportunity to develop due to the high morphodynamics. In general, debris flows are probably
655 the most common processes, although it is difficult to separate the different processes, but very high sediment yield (mainly
656 in the first time period) also indicate landslides and slope failures. Site morphodynamic is also related to the characteristics,
657 i.e. sites that are larger, have longer max. lengths and higher mean slope gradients (as well as max. slope gradients) have
658 clearly higher geomorphic activity and form more deeply incised gullies. In the sense of a process-response system, it can be
659 stated that the melting of dead ice in the lower slope area, which in some cases lasts for decades, leads to high morphodynamics
660 of the upper slope area. Furthermore, it is assumed that the lowering of the erosion base by adjacent streams leads to a delay
661 of the paraglacial landscape adjustment, as the formation of an accumulation area is disrupted.
662 In addition to the system-internal influences on morphodynamics, we assume an additional influence of changing weather and
663 climate factors on the corresponding erosion processes with an increase (mainly in the last, i.e. most recent time period from
664 the mid-2000s to 2017/2019), since the statistically significant warming of the last decades has led to a reduction of the mean
665 annual ice days, to an increase in warm air inflows and, when distinguishing between rainfall and snowfall, to an increase in
666 rainfall. We do not see any clear influence in the changing precipitation, although it can be assumed that the same precipitation
667 intensities led to higher erosion in the first time period than in the second or third. Nevertheless, the system-internal dynamics
668 and the general paraglacial adaptation process seem to have the greatest impact on the changing morphodynamics. Future work
669 should apply the approach used here to more areas and, if possible, with a higher temporal resolution to improve the process
670 understanding of erosion on lateral moraines.



672
673 **Boxplots of the model parameters Intercept, Slope and R² of all regression lines (see Figure 6).**

675 Calculation of the individual extreme events by continuous ongoing 4 mm classes (with one-hour resolution).

	Precipitation interval (mm)	No. events/total	No. events/year	No. events/total	No. events/year	No. events/total	No. events/year	Change from previous time period	
Grastalferner (Horlachtal)		1954-1973 (period I)		1973-2006 (period II)		2006-2015 (period III)		I to II	II to III
	>0 to 4	6084	304.20	10315	303.38	3005	300.50	-0.82	-2.88
	4 to 8	368	18.40	615	18.09	184	18.40	-0.31	-0.31
	8 to 12	78	3.90	124	3.65	49	4.90	-0.25	1.25
	12 to 16	17	0.85	33	0.97	12	1.20	0.12	0.23
	16 to 20	7	0.35	13	0.38	4	0.40	0.03	0.02
	20 to 24	2	0.10	8	0.24	2	0.20	0.14	-0.04
	24 to 28	1	0.05	2	0.06	1	0.10	0.01	0.04
	>28	1	0.05	1	0.03	0	0.00	-0.02	-0.03
Gepatschferner (Kaunertal)		1953-1971 (period I)		1971-2006 (period II)		2006-2015 (period III)		I to II	II to III
	>0 to 4	5498	289.37	10278	285.50	2912	291.20	-3.87	5.70
	4 to 8	390	20.53	700	19.44	247	24.70	-1.09	5.26
	8 to 12	87	4.58	178	4.94	47	4.70	0.36	-0.24
	12 to 16	20	1.05	44	1.22	14	1.40	0.17	0.18
	16 to 20	9	0.47	15	0.42	4	0.40	-0.05	-0.02
	20 to 24	3	0.16	9	0.25	1	0.10	0.09	-0.15
	24 to 28	1	0.05	1	0.03	0	0.00	-0.02	-0.03
	>28	1	0.05	0	0.00	0	0.00	-0.05	0.00
Gepatschferner/ Müchner/ Abfahrt (Kaunertal)		1953-1971 (period I)		1971-2006 (period II)		2006-2015 (period III)		I to II	II to III
	>0 to 4	5452	286.95	10316	286.56	2856	285.60	-0.39	-0.96
	4 to 8	402	21.16	750	20.83	249	24.90	-0.33	4.07
	8 to 12	96	5.05	165	4.58	51	5.10	-0.47	0.52
	12 to 16	23	1.21	41	1.14	10	1.00	-0.07	-0.14
	16 to 20	4	0.21	8	0.22	4	0.40	0.01	0.18
	20 to 24	1	0.03	6	0.17	2	0.20	0.14	0.03
	24 to 28	2	0.11	1	0.03	0	0.00	-0.08	-0.03
Weißseeferner (Kaunertal)		1953-1971 (period I)		1971-2006 (period II)		2006-2015 (period III)		I to II	II to III
	>0 to 4	5690	299.74	10580	293.89	2931	293.10	-5.85	0.79
	4 to 8	408	21.47	745	20.69	251	25.10	-0.78	4.41
	8 to 12	96	5.05	166	4.61	56	5.60	-0.44	0.99
	12 to 16	23	1.21	44	1.22	7	0.70	0.01	-0.52
	16 to 20	9	0.47	14	0.39	5	0.50	-0.08	0.11
	20 to 24	2	0.11	8	0.22	2	0.20	0.11	-0.02
Hohenferner (Martelltal)		1959-2005 (period I)		2005-2015 (period II)				I to II	
	>0 to 4	14531	302.73			3405	309.55	6.82	
	4 to 8	883	18.40			228	20.73	2.33	
	8 to 12	241	5.02			59	5.36	0.34	
	12 to 16	57	1.19			17	1.55	0.36	
	16 to 20	8	0.17			2	0.18	0.01	
	20 to 24	3	0.06			1	0.09	0.03	
	24 to 28	3	0.06			0	0.00	-0.06	

678 Calculation of the daily precipitation totals by continuous ongoing 4 mm classes of the different time periods (24-hour resolution).

Glacier foreland	Precipitation interval (mm)	No. events/ total	No. events/ year	No. events/ total	No. events/ year	No. events/ total	No. events/year	Change from previous period	
Grastalferner		1954-1973 (epoch I)		1973-2006 (epoch II)		2006-2015 (epoch III)		I to II	II to III
(Horlachtal)	0 to 10	410	20.50	732	21.53	228	22.80	1.03	1.27
	10 to 20	181	9.05	341	10.03	114	11.40	0.98	1.37
	20 to 30	113	5.65	191	5.62	46	4.60	-0.03	-1.02
	30 to 40	47	2.35	101	2.97	35	3.50	0.62	0.53
	40 to 50	26	1.30	35	1.03	8	0.80	-0.27	-0.23
	50 to 60	13	0.65	14	0.41	6	0.60	-0.24	0.19
	60 to 70	0	0.00	6	0.18	1	0.10	0.18	-0.08
	>70	2	0.10	0	0.00	1	0.10	-0.10	0.10
Gepatschferner		1953-1971 (period I)		1971-2006 (period II)		2006-2017 (period III)		I to II	II to III
(Kaunertal)	0 to 10	335	17.63	706	19.61	192	19.20	1.98	-0.44
	10 to 20	174	9.16	325	9.03	95	9.50	-0.13	0.47
	20 to 30	105	5.53	224	6.22	61	6.10	0.69	-0.12
	30 to 40	73	3.84	107	2.97	34	3.40	-0.87	0.43
	40 to 50	22	1.16	50	1.39	18	1.80	0.23	0.41
	50 to 60	11	0.58	19	0.53	4	0.40	-0.05	-0.13
	60 to 70	5	0.26	11	0.31	1	0.10	0.05	-0.21
	70 to 80	2	0.11	3	0.08	0	0.00	-0.03	-0.08
	80 to 90	0	0.00	2	0.06	0	0.00	0.06	-0.06
	90 to 100	0	0.00	5	0.14	2	0.20	0.14	0.06
	>100	4	0.21	5	0.14	0	0.00	-0.07	-0.14
Gepatschferner/ Müchner Abfahrt (Kaunertal)		1953-1971 (period I)		1971-2006 (period II)		2006-2017 (period III)		I to II	II to III
	0 to 10	304	16.00	618	17.17	168	16.80	1.17	-0.37
	10 to 20	146	7.68	301	8.36	81	8.10	0.68	-0.26
	20 to 30	101	5.32	197	5.47	57	5.70	0.15	0.23
	30 to 40	69	3.63	115	3.19	34	3.40	-0.44	0.21
	40 to 50	35	1.84	50	1.39	20	2.00	-0.45	0.61
	50 to 60	12	0.63	26	0.72	6	0.60	0.09	-0.12
	60 to 70	5	0.26	12	0.33	1	0.10	0.07	-0.23
	70 to 80	1	0.05	5	0.14	0	0.00	0.09	-0.14
	>80	4	0.21	10	0.28	2	0.20	0.07	-0.08
Weißseeferner (Kaunertal)		1953-1971 (period I)		1971-2006 (period II)		2006-2017 (period III)		I to II	II to III
	0 to 10	302	15.89	623	17.31	179	17.90	1.42	0.59
	10 to 20	146	7.68	296	8.22	88	8.80	0.54	0.58
	20 to 30	99	5.21	203	5.64	53	5.30	0.43	-0.34
	30 to 40	75	3.95	104	2.89	32	3.20	-1.06	0.31
	40 to 50	32	1.68	46	1.28	18	1.80	-0.40	0.52
	50 to 60	12	0.63	28	0.78	6	0.60	0.15	-0.18
	60 to 70	3	0.16	14	0.39	1	0.10	0.23	-0.29
	70 to 80	1	0.05	3	0.08	1	0.10	0.03	0.02
	80 to 90	1	0.05	4	0.11	1	0.10	0.06	-0.01
	>90	3	0.16	6	0.17	0	0.00	0.01	-0.17
Hohenferner (Martelltal)		1959-2005 (period I)				2005-2019 (period II)		I to II	
	0 to 10	1169	24.35			323	29.36	5.01	

10 to 20	403	8.40	105	9.55	1.15
20 to 30	241	5.02	40	3.64	-1.38
30 to 40	127	2.65	31	2.82	0.17
40 to 50	54	1.13	15	1.36	0.23
50 to 60	27	0.56	9	0.82	0.26
60 to 70	38	0.79	8	0.73	-0.06
70 to 80	16	0.33	3	0.27	-0.06
80 to 90	24	0.50	5	0.45	-0.05
90 to 100	5	0.10	3	0.27	0.17
100 to 110	5	0.10	1	0.09	-0.01
110 to 120	5	0.10	0	0.00	-0.10
120 to 130	4	0.08	1	0.09	0.01
130 to 140	5	0.10	0	0.00	-0.10

679 **Code availability**

680 The processing of the historical aerial images into point clouds (and orthophotos) was done with the commercial software
681 Agisoft Metashape Professional (Version 1.6.6). These point clouds as well as the point clouds based on LiDAR data (ALS)
682 were further processed in the commercial geoinformation system SAGA LIS Pro 3D (Version 7.4.0) and converted into DEMs.
683 The preparatory steps for the regression lines (derivation of the corresponding value pairs (sediment yield and sediment
684 contributing area)) were carried out in open-source software SAGA GIS (Version 7.2.0), whereby the subsequent automated
685 repetition of the extraction of the value pairs by using a for-loop and the calculation of the corresponding regression lines were
686 carried out in the open-source software R (RStudio, version 1.4.1103). Maps were created in both the open-source software
687 SAGA GIS and QGIS (Version 3.22.4). Atmospheric simulation was performed using the Advanced Research version of the
688 Weather Research and Forecasting (ARW-WRF) model (version 4.3). The meteorological analyses were carried out in R.

689 **Data availability**

690 The historical aerial images and the corresponding calibration certificates (if available) were provided by the Federal Office
691 of Metrology and Surveying (BEV, Vienna, Austria) (aerial image series 1953 and 1954), by the Italian Military Geographic
692 Institute (IGMI, Florence, Italy) (aerial image series 1945 and 1959) and by the Province of Tyrol (aerial image series 1970,
693 1971 and 1973). The DEM 2006 (Horlachtal) and the point clouds of 2006 and 2004/2005 (Kaunertal and Martelltal) were
694 provided by the Province of Tyrol and the Autonomous Province of Bolzano. The historical maps of 1886/1887 (Kaunertal),
695 1889 (Horlachtal), 1918 (Martelltal) and 1922 (Kaunertal) were provided by the Archive of the German Alpine Club (DAV),
696 the Ötztal Gedächtnisspeicher (Längenfeld, Austria), the BEV and the Bavarian Academy of Sciences and Humanities. The
697 orthophotos of 2020 (all valleys) were made available for download by the Province of Tyrol and the Autonomous Province
698 of Bolzano on their respective websites. The large-scale elevation data (DSM and Hillshade) (Overview European Alps, Figure
699 1) was provided by Copernicus (Copernicus Land Monitoring Service). These data were produced with the financial support
700 of the European Union. The 20th century NOAA/CIRES/DOE reanalysis data (V3) were provided by NOAA PSL, Boulder,

701 Colorado, USA, from their website <https://psl.noaa.gov>. Support for the Twentieth Century Reanalysis Project version 3 dataset
702 is provided by the U.S. Department of Energy, Office of Science Biological and Environmental Research (BER), by the
703 National Oceanic and Atmospheric Administration Climate Program Office, and by the NOAA Earth System Research
704 Laboratory Physical Sciences Laboratory. Δ8364.

705 **Author contribution**

706 The study was conceptualised by MA, FH, TH and MB. Data preparation was carried out by MA, JR, FF, FH, LP, MP, MW,
707 LB, MS and SB-N. The methodological approach was developed by MA, JR, FH and TH for the sediment contributing area
708 modelling and MA, FH and MP for the meteorological analysis. The formal analysis was carried out by MA and MP.
709 Supervision was carried out by FH, TH and MB. The original draft was prepared by MA. JR, FF, FH, TH, LP, MP, MW, LB,
710 MS, SB-N and MB were involved in the revision of the manuscript. MB, FH and TH were responsible for fundraising and
711 project management.

712 **Competing interests**

713 The authors declare that they have no conflict of interest.

714 **Acknowledgement**

715 We would like to thank the German Research Foundation (DFG), the Austrian Science Fund (FWF) and the Swiss National
716 Science Foundation (SNF) for financial support of the research project SEHAG (SEnsitivity of High Alpine Geosystems to
717 climate change since 1850), within the framework of which this study was generated. Furthermore, we would like to thank for
718 providing the aerial images and the calibration certificates. In this context, we would like to thank the BEV, IGMI, the Province
719 of Tyrol, the Province of Bolzano and the Hydrographic Office of the Autonomous Province of Bolzano (Civil Protection
720 Agency). In addition, we would also like to thank the Province of Tyrol for providing the DEM 2006 (Horlachtal) as well as
721 the point cloud 2006 (Kaunertal) and the Autonomous Province of Bolzano for the point cloud 2006 (Martelltal). We would
722 also like to thank the Archive of the German Alpine Club (DAV), the Ötztaler Gedächtnisspeicher, the BEV and the Bavarian
723 Academy of Sciences and Humanities for providing the historical maps 1886/1887 (Kaunertal), 1889 (Horlachtal), 1918
724 (Martelltal) and 1922 (Kaunertal). We would also like to thank the Province of Tyrol and the Autonomous Province of Bolzano
725 for the orthophotos of 2020, which can be downloaded on their websites quickly and easily. We would also like to thank
726 Copernicus (Copernicus Land Monitoring Service) for the available download of the coarse resolution hillshade (Overview
727 European Alps, Figure 1). Additionally, we would like to thank Wucher Helikopter GmbH (Ludesch, Austria) for carrying out
728 the flights in which the LiDAR data (ALS) 2017 (Kaunertal) and 2019 (Horlachtal and Martelltal) were acquired. Many thanks

729 for the safe flights even in difficult high alpine terrain. In addition, many thanks to NOAA PSL, Boulder, Colorado, USA for
730 the 20CRv3 dataset.

731 **Funding**

732 The study was financially supported by the German Research Foundation (DFG) and the Austrian Science Fund (FWF) (grant
733 numbers: BE 1118/38-1, BE 1118/39-1, BE 1118/40-1, HA 5740/10-1, HE 5747/6-1, MA 6966/4-1, LA 4426/1-1 and 4062-
734 N29). The open access publication of this article was supported by the Open Access Fund of the Catholic University of
735 Eichstätt-Ingolstadt.

736 **References**

- 737 Altmann, M., Piermattei, L., Haas, F., Heckmann, T., Fleischer, F., Rom, J., Betz-Nutz, S., Knoflach, B., Müller, S.,
738 Ramskogler, K., Pfeiffer, M., Hofmeister, F., Ressler, C., and Becht, M.: Long-Term Changes of Morphodynamics on
739 Little Ice Age Lateral Moraines and the Resulting Sediment Transfer into Mountain Streams in the Upper Kauner
740 Valley, Austria, *Water*, 12, 3375, <https://doi.org/10.3390/w12123375>, 2020.
- 741 Altmann, M., Haas, F., Heckmann, T., Liébault, F., and Becht, M.: Modelling of sediment supply from torrent catchments in
742 the Western Alps using the sediment contributing area (SCA) approach, *Earth Surf. Process. Landforms*, 46, 889–906,
743 <https://doi.org/10.1002/esp.5046>, 2021.
- 744 Anderson, S. W.: Uncertainty in quantitative analyses of topographic change: error propagation and the role of thresholding,
745 *Earth Surf. Process. Landforms*, 44, 1015–1033, <https://doi.org/10.1002/esp.4551>, 2019.
- 746 Bakker, M. and Lane, S.: Archival photogrammetric analysis of river-floodplain systems using Structure from Motion (SfM)
747 methods, *Earth Surf. Process. Landforms*, 42, 1274–1286, <https://doi.org/10.1002/esp.4085>, 2017.
- 748 Ballantyne, C. K.: A general model of paraglacial landscape response, *The Holocene*, 12, 371–376,
749 <https://doi.org/10.1191/0959683602hl553fa>, 2002a.
- 750 Ballantyne, C. K.: Paraglacial geomorphology, *Quaternary Science Reviews*, 21, 1935–2017, [https://doi.org/10.1016/S0277-
751 3791\(02\)00005-7](https://doi.org/10.1016/S0277-3791(02)00005-7), 2002b.
- 752 Ballantyne, C. K. and Benn, D. I.: Paraglacial slope adjustment during recent deglaciation and its implications for slope
753 evolution in formerly glaciated environments, Anderson, M. G., & Brooks, S. M. (eds.), *Advances in hillslope processes*,
754 2, 1173–1195, 1996.
- 755 Ballantyne, C. K. and Benn, D. I.: Paraglacial Slope Adjustment and Resedimentation following Recent Glacier Retreat,
756 Fåbergstølsdalen, Norway, *Arctic and Alpine Research*, 26, 255–269, 1994.
- 757 Becht, M.: Untersuchungen zur aktuellen Reliefentwicklung in alpinen Einzugsgebieten, Univ., Habil.-Schr, Münchener
758 Universitätsschriften/Fakultät für Geowissenschaften, 47, Geobuch-Verl., Germany, München, 187 pp., 1995.

- 759 Beniston, M., Farinotti, D., Stoffel, M., Andreassen, L. M., Coppola, E., Eckert, N., Fantini, A., Giacona, F., Hauck, C.,
760 Huss, M., Huwald, H., Lehning, M., López-Moreno, J.-I., Magnusson, J., Marty, C., Morán-Tejeda, E., Morin, S.,
761 Naaim, M., Provenzale, A., Rabatel, A., Six, D., Stötter, J., Strasser, U., Terzago, S., and Vincent, C.: The European
762 mountain cryosphere: a review of its current state, trends, and future challenges, *The Cryosphere*, 12, 759–794,
763 <https://doi.org/10.5194/tc-12-759-2018>, 2018.
- 764 Besl, P. J. and McKay, N. D.: Method for registration of 3-D shapes, in: *Sensor Fusion IV: Control Paradigms and Data*
765 *Structures*, Boston, MA, Friday 1 November 1991, 586–606, 1992.
- 766 Betz, S., Croce, V., and Becht, M.: Investigating morphodynamics on Little Ice Age lateral moraines in the Italian Alps
767 using archival aerial photogrammetry and airborne LiDAR data, *Zeitschrift für Geomorphologie*, 62, 231–247,
768 <https://doi.org/10.1127/zfg/2019/0629>, 2019.
- 769 Betz-Nutz, S.: Vergleichende photogrammetrische Untersuchungen zu langfristigen Veränderungen der Morphodynamik auf
770 neuzeitlichen Lateralmoränen ausgewählter Alpengletscher, Dissertation, Universitätsbibliothek Eichstätt-Ingolstadt,
771 Eichstätt, 2021.
- 772 Betz-Nutz, S., Heckmann, T., Haas, F., and Becht, M.: Development of the morphodynamics on Little Ice Age lateral
773 moraines in 10 glacier forefields of the Eastern Alps since the 1950s, *Earth Surf. Dynam.*, 11, 203–226,
774 <https://doi.org/10.5194/esurf-11-203-2023>, 2023.
- 775 Blair, R. W.: Moraine and Valley Wall Collapse due to Rapid Deglaciation in Mount Cook National Park, New Zealand,
776 *Mountain Research and Development*, 14, 347, <https://doi.org/10.2307/3673731>, 1994.
- 777 Brugnara, Y., Brunetti, M., Maugeri, M., Nanni, T., and Simolo, C.: High-resolution analysis of daily precipitation trends in
778 the central Alps over the last century, *Int. J. Climatol.*, 32, 1406–1422, <https://doi.org/10.1002/joc.2363>, 2012.
- 779 Carrivick, J. L., Geilhausen, M., Warburton, J., Dickson, N. E., Carver, S. J., Evans, A. J., and Brown, L. E.: Contemporary
780 geomorphological activity throughout the proglacial area of an alpine catchment, *Geomorphology*, 188, 83–95,
781 <https://doi.org/10.1016/j.geomorph.2012.03.029>, 2013.
- 782 Cavalli, M., Goldin, B., Comiti, F., Brardinoni, F., and Marchi, L.: Assessment of erosion and deposition in steep mountain
783 basins by differencing sequential digital terrain models, *Geomorphology*, 291, 4–16,
784 <https://doi.org/10.1016/j.geomorph.2016.04.009>, 2017.
- 785 Chen, F. and Dudhia, J.: Coupling an Advanced Land Surface–Hydrology Model with the Penn State–NCAR MM5
786 Modeling System. Part II: preliminary model validation, *Mon. Wea. Rev.*, 129, 569–585, [https://doi.org/10.1175/1520-0493\(2001\)129<0569:CAALSH>2.0.CO;2](https://doi.org/10.1175/1520-0493(2001)129<0569:CAALSH>2.0.CO;2), 2001.
- 788 Church, M. and Ryder, J. M.: Paraglacial Sedimentation: A Consideration of Fluvial Processes Conditioned by Glaciation,
789 *Geol Soc America Bull*, 83, 3059, [https://doi.org/10.1130/0016-7606\(1972\)83\[3059:PSACOF\]2.0.CO;2](https://doi.org/10.1130/0016-7606(1972)83[3059:PSACOF]2.0.CO;2), 1972.
- 790 Cody, E., Anderson, B. M., McColl, S. T., Fuller, I. C., and Purdie, H. L.: Paraglacial adjustment of sediment slopes during
791 and immediately after glacial debuitressing, *Geomorphology*, 371, 107411,

792 <https://doi.org/10.1016/j.geomorph.2020.107411>, available at:
793 <https://www.sciencedirect.com/science/article/pii/S0169555X20303846>, 2020.

794 Collier, E. and Mölg, T.: BAYWRF: a high-resolution present-day climatological atmospheric dataset for Bavaria, Earth
795 Syst. Sci. Data, 12, 3097–3112, <https://doi.org/10.5194/essd-12-3097-2020>, 2020.

796 Collier, E., Sauter, T., Mölg, T., and Hardy, D.: The Influence of Tropical Cyclones on Circulation, Moisture Transport, and
797 Snow Accumulation at Kilimanjaro During the 2006–2007 Season, *J. Geophys. Res. Atmos.*, 124, 6919–6928,
798 <https://doi.org/10.1029/2019JD030682>, 2019.

799 Compo, G. P., Whitaker, J. S., Sardeshmukh, P. D., Matsui, N., Allan, R. J., Yin, X., Gleason, B. E., Vose, R. S., Rutledge,
800 G., Bessemoulin P., Brönnimann, S., Brunet, M., Crouthamel, R. I., Grant, A. N., Groisman, P. Y., Jones, P. D., Kruk,
801 M., Kruger, A. C., Marshall, G. J., Maugeri, M., Mok, H. Y., Nordli, Ø., Ross, T. F., Trigo, R. M., Wang, X. L.,
802 Woodruff, S. D., and Worley, S. J.: The Twentieth Century Reanalysis Project, *Quarterly J. Roy. Meteorol. Soc.*, 137, 1–
803 28, 2011.

804 Conrad, O., Bechtel, B., Bock, M., Dietrich, H., Fischer, E., Gerlitz, L., Wehberg, J., Wichmann, V., and Böhner, J.: System
805 for Automated Geoscientific Analyses (SAGA) v. 2.1.4, *Geoscientific Model Development*, 8, 1991–2007, 2015.

806 Copernicus: Hillshade derived from EU-DEM version 1.0, [https://land.copernicus.eu/imagery-in-situ/eu-dem/eu-dem-v1-0-](https://land.copernicus.eu/imagery-in-situ/eu-dem/eu-dem-v1-0-and-derived-products/hillshade?tab=metadata)
807 [and-derived-products/hillshade?tab=metadata](https://land.copernicus.eu/imagery-in-situ/eu-dem/eu-dem-v1-0-and-derived-products/hillshade?tab=metadata), last access: 3 June 2021, 2016.

808 Curry, A. M.: Paraglacial modification of slope form, *Earth Surf. Process. Landforms*, 24, 1213–1228,
809 [https://doi.org/10.1002/\(SICI\)1096-9837\(199912\)24:13<1213:AID-ESP32>3.0.CO;2-B](https://doi.org/10.1002/(SICI)1096-9837(199912)24:13<1213:AID-ESP32>3.0.CO;2-B), 1999.

810 Curry, A. M., Cleasby, V., and Zukowskyj, P.: Paraglacial response of steep, sediment-mantled slopes to post-‘Little Ice
811 Age’ glacier recession in the central Swiss Alps, *J. Quaternary Sci.*, 21, 211–225, <https://doi.org/10.1002/jqs.954>, 2006.

812 Curry, A. M., Sands, T. B., and Porter, P. R.: Geotechnical controls on a steep lateral moraine undergoing paraglacial slope
813 adjustment, *Geological Society, London, Special Publications*, 320, 181–197, <https://doi.org/10.1144/SP320.12>, 2009.

814 Deline, P., Gruber, S., Delaloye, R., Fischer, L., Geertsema, M., Giardino, M., Hasler, A., Kirkbride, M., Krautblatter, M.,
815 Magnin, F., McColl, S., Ravel, L., and Schoeneich, P.: Chapter 15 - Ice Loss and Slope Stability in High-Mountain
816 Regions, in: Shroder, J.F; Haeberli, W; Whiteman, C; Hazards and Disasters Series, *Snow and Ice-Related Hazards,*
817 *Risks, and Disasters*, Academic press, 521–561, <https://doi.org/10.1016/B978-0-12-394849-6.00015-9>.

818 Draebing, D. and Eichel, J.: Spatial Controls of Turf-Banked Solifluction Lobes and Their Role for Paraglacial Adjustment
819 in Glacier Forelands, *Permafrost and Periglacial Processes*, 28, 446–459, <https://doi.org/10.1002/ppp.1930>, 2017.

820 Dusik, J.: Die aktuelle Geomorphodynamik auf proglazialen Moränen im Hinteren Kaunertal: Hochaufgelöste Messung und
821 Modellierung der Prozessdynamik hinsichtlich ihrer lokalen und temporalen Variabilität, *Dissertation, Katholische*
822 *Universität Eichstätt-Ingolstadt, Eichstätt*, 2019.

823 Dusik, J.-M., Neugirg, F., and Haas, F.: Slope Wash, Gully Erosion and Debris Flows on Lateral Moraines in the Upper
824 Kaunertal, Austria, in: *Geomorphology of Proglacial Systems*, Springer, Cham, 177–196, [https://doi.org/10.1007/978-3-](https://doi.org/10.1007/978-3-319-94184-4_11)
825 [319-94184-4_11](https://doi.org/10.1007/978-3-319-94184-4_11), 2019.

826 Eichel, J., Corenblit, D., and Dikau, R.: Conditions for feedbacks between geomorphic and vegetation dynamics on lateral
827 moraine slopes: a biogeomorphic feedback window, *Earth Surface Processes and Landforms*, 41, 406–419,
828 <https://doi.org/10.1002/esp.3859>, 2016.

829 Eichel, J., Draebing, D., Winkler, S., and Meyer, N.: Similar vegetation-geomorphic disturbance feedbacks shape unstable
830 glacier forelands across mountain regions, *Ecosphere*, 14, <https://doi.org/10.1002/ecs2.4404>, 2023.

831 Eltner, A., Kaiser, A., Castillo, C., Rock, G., Neugirg, F., and Abellán, A.: Image-based surface reconstruction in
832 geomorphometry – merits, limits and developments, *Earth Surf. Dynam.*, 4, 359–389, [https://doi.org/10.5194/esurf-4-](https://doi.org/10.5194/esurf-4-359-2016)
833 [359-2016](https://doi.org/10.5194/esurf-4-359-2016), 2016.

834 Fehlmann, M., Gascón, E., Rohrer, M., Schwarb, M., and Stoffel, M.: Estimating the snowfall limit in alpine and pre-alpine
835 valleys: A local evaluation of operational approaches, *Atmospheric Research*, 204, 136–148,
836 <https://doi.org/10.1016/j.atmosres.2018.01.016>, 2018.

837 Finsterwalder, S.: Begleitworte zur Karte des Gepatschferners, *Zeitschrift für Gletscherkunde XVI (1/2)*, 20–41, 1928.

838 Finsterwalder, S. and Schunck, H.: Die Zunge des Gepatschferners 1886/87, *Zeitschrift des Deutschen und*
839 *Oesterreichischen Alpenvereins*, Tafel 4, 1888.

840 Fleischer, F., Haas, F., Piermattei, L., Pfeiffer, M., Heckmann, T., Altmann, M., Rom, J., Stark, M., Wimmer, H. W., Pfeifer,
841 N., and Becht, M.: Multi-decadal (1953–2017) rock glacier kinematics analysed by high-resolution topographic data in
842 the upper Kaunertal, Austria, *The Cryosphere*, 15, 5345–5369, <https://doi.org/10.5194/tc-15-5345-2021>, 2021.

843 Froidurot, S., Zin, I., Hingray, B., and Gautheron, A.: Sensitivity of Precipitation Phase over the Swiss Alps to Different
844 Meteorological Variables, *Journal of Hydrometeorology*, 15, 685–696, <https://doi.org/10.1175/JHM-D-13-073.1>,
845 available at: https://journals.ametsoc.org/view/journals/hydr/15/2/jhm-d-13-073_1.xml, 2014.

846 Fryirs, K.: (Dis)Connectivity in catchment sediment cascades: a fresh look at the sediment delivery problem, *Earth Surf.*
847 *Process. Landforms*, 38, 30–46, <https://doi.org/10.1002/esp.3242>, 2013.

848 Fryirs, K. A., Brierley, G. J., Preston, N. J., and Spencer, J.: Catchment-scale (dis)connectivity in sediment flux in the upper
849 Hunter catchment, New South Wales, Australia, *Geomorphology*, 84, 297–316,
850 <https://doi.org/10.1016/j.geomorph.2006.01.044>, 2007.

851 Geitner, C.: Sedimentologische und vegetationsgeschichtliche Untersuchungen an fluvialen Sedimenten in den Hochlagen
852 des Horlachteles (Stubai Alpen, Tirol): ein Beitrag zur zeitlichen Differenzierung der fluvialen Dynamik im Holozän,
853 vol. 31 of *Münchener Geographische Abhandlungen A*, Geobuch-Verlag, Diss., München, 1999.

854 Geological Survey of Austria: Geological map of Austria, 1:2.000.000, Vienna, 1999.

855 Giese, B. S., Seidel, H. F., Compo, G. P., and Sardeshmukh, P. D.: An ensemble of ocean reanalyses for 1815–2013 with
856 sparse observational input, *J. Geophys. Res. Oceans*, 121, 6891–6910, <https://doi.org/10.1002/2016JC012079>, 2016.

857 Gomez, C., Hayakawa, Y., and Obanawa, H.: A study of Japanese landscapes using structure from motion derived DSMs
858 and DEMs based on historical aerial photographs: New opportunities for vegetation monitoring and diachronic
859 geomorphology, *Geomorphology*, 242, 11–20, <https://doi.org/10.1016/j.geomorph.2015.02.021>, 2015.

860 Groß, G. and Patzelt, G.: The Austrian Glacier Inventory for the Little Ice Age Maximum (GI LIA) in ArcGIS (shapefile)
861 format, 2015.

862 Haas, F.: Fluviale Hangprozesse in alpinen Einzugsgebieten der nördlichen Kalkalpen: Quantifizierung und
863 Modellierungsansätze, Dissertation, Katholische Universität Eichstätt-Ingolstadt, Eichstätt, 2008.

864 Haas, F., Heckmann, T., Hilger, L., and Becht, M.: Quantification and Modelling of Debris Flows in the Proglacial Area of
865 the Gepatschferner/Austria using Ground-based LIDAR, Collins, Adrian L. ; Golosov, Valentin ; Horowitz, Arthur J. ;
866 Lu, Xixi ; Stone, Mike ; Walling, Des E. ; Zhang, Xinbao (Eds.): Erosion and Sediment Yields in the Changing
867 Environment: proceedings of an IAHS International Commission on Continental Erosion Symposium, held at the
868 Institute of Mountain Hazards and Environment, CAS-Chengdu, China, 11-15 October 2012, IAHS publication, 356,
869 293–302, 2012.

870 Haas, F., Heckmann, T., Wichmann, V., and Becht, M.: Quantification and Modeling of Fluvial Bedload Discharge from
871 Hillslope Channels in two Alpine Catchments (Bavarian Alps, Germany), *Zeitschrift für Geomorphologie N.F. Suppl.*,
872 55, 147–168, <https://doi.org/10.1127/0372-8854/2011/0055S3-0056>, 2011.

873 Haeberli, W. and Whiteman, C.: *Snow and Ice-Related Hazards, Risks, and Disasters*, Elsevier, 2021.

874 Hagg, W. and Becht, M.: Einflüsse von Niederschlag und Substrat auf die Auslösung von Hangmuren in Beispielgebieten
875 der Ostalpen, *Zeitschrift für Geomorphologie*, 79–92, 2000.

876 Haselberger, S., Zangerl, U., Scheper, S., Otto, J.-C., Ohler, L.-M., Junker, R. R., and Kraushaar, S.: Catchment-Scale
877 Stability and Disturbance in Biogeomorphic Succession in an Alpine Glacier Foreland (Kaunertal Valley, Austria),
878 *SSRN Journal*, <https://doi.org/10.2139/ssrn.4202209>, 2022.

879 Haselberger, S., Ohler, L.-M., Junker, R. R., Otto, J.-C., Glade, T., and Kraushaar, S.: Quantification of biogeomorphic
880 interactions between small-scale sediment transport and primary vegetation succession on proglacial slopes of the
881 Gepatschferner, Austria, *Earth Surf. Process. Landforms*, 46, 1941–1952, <https://doi.org/10.1002/esp.5136>, 2021.

882 Heckmann, T. and Vericat, D.: Computing spatially distributed sediment delivery ratios: inferring functional sediment
883 connectivity from repeat high-resolution digital elevation models, *Earth Surf. Process. Landforms*, 43, 1547–1554,
884 <https://doi.org/10.1002/esp.4334>, 2018.

885 Heckmann, T. and Morche, D. (Eds.): *Geomorphology of proglacial systems: Landform and sediment dynamics in recently
886 deglaciated alpine landscapes*, *Geography of the Physical Environment*, Springer International Publishing, Cham,
887 Switzerland, 2019.

888 Heinimann, H., Hollenstein, K., Kienholz, H., Krummenacher, B., and Mani, P.: *Methoden zur Analyse und Bewertung von
889 Naturgefahren*, 85, *Umwelt-Materialien, BUWAL - Bundesamt für Umwelt, Wald und Landschaft*, Bern, 1998.

890 Hersbach, H., Bell, B., Berrisford, P., Biavati, G., Horányi, A., Muñoz Sabater, J., Nicolas, J., Peubey, C., Radu, R., Rozum,
891 I., Schepers, D., Simmons, A., Soci, C., Dee, D., and Thépaut, J.-N.: ERA5 hourly data on single levels from 1979 to
892 present: Copernicus Climate Change Service (C3S) Climate Data Store (CDS), <https://doi.org/10.24381/cds.adbb2d47>,
893 last access: 13 October 2021, 2018.

894 Hilger, L.: Quantification and regionalization of geomorphic processes using spatial models and high-resolution topographic
895 data: A sediment budget of the Upper Kauner Valley, Ötztal Alps., Dissertation, Katholische Universität Eichstätt-
896 Ingolstadt, Eichstätt, 2017.

897 Hock, R., Rasul, G., Adler, C., Cáceres, B., Gruber, S., Hirabayashi, Y.: Jackson, M., Kääb, A., Kang, S., Kutuzov, S., and
898 Milner, A. L.: High Mountain Areas: In: IPCC Special Report on the Ocean and Cryosphere in a Changing Climate [H.-
899 O. Pörtner, D.C. Roberts, V. Masson-Delmotte, P. Zhai, M. Tignor, E. Poloczanska, K. Mintenbeck, A. Alegría, M.
900 Nicolai, A. Okem, J. Petzold, B. Rama, N.M. Weyer (eds.)]. Cambridge University Press, Cambridge, UK and New
901 York, NY, USA, 131–202, <https://doi.org/10.1017/9781009157964.004>, 2019.

902 Hodgson, M. E. and Bresnahan, P.: Accuracy of Airborne Lidar-Derived Elevation, <https://doi.org/10.14358/PERS.70.3.331>,
903 2004.

904 Hong, S. Y., Noh, Y., and Dudhia, J.: A new vertical diffusion package with an explicit treatment of entrainment processes,
905 *Mon. Weather Rev.*, 134, 2318–2341, <https://doi.org/10.1175/MWR3199.1>, 2006.

906 Huber, A., Heckmann, T., Haas, F., and Becht, M.: DEM-based scaling of bedload sediment yield in low-order torrents of
907 the Isar catchment, In: *Guidelines for Assessing Sediment Dynamics in Alpine Basins and Channel Reaches: Final*
908 *Report of the SedAlp Project, Work Package 4. SedAlp, Vienna; Annex 39-46*, 2015.

909 Hugenholtz, C. H., Moorman, B. J., Barlow, J., and Wainstein, P. A.: Large-scale moraine deformation at the Athabasca
910 Glacier, Jasper National Park, Alberta, Canada, *Landslides*, 5, 251–260, <https://doi.org/10.1007/s10346-008-0116-5>,
911 2008.

912 Iacono, M. J., Delamere, J. S., Mlawer, E. J., Shephard, M. W., Clough, S. A., and Collins, W. D.: Radiative forcing by long-
913 lived greenhouse gases: Calculations with the AER radiative transfer models, *J. Geophys. Res.*, 113,
914 <https://doi.org/10.1029/2008JD009944>, 2008.

915 IPCC: *Climate Change 2021: The Physical Science Basis. Contribution of Working Group I to the Sixth Assessment Report*
916 *of the Intergovernmental Panel on Climate Change [Masson-Delmotte, V., P. Zhai, A. Pirani, S.L. Connors, C. Péan, S.*
917 *Berger, N. Caud, Y. Chen, L. Goldfarb, M.I. Gomis, M. Huang, K. Leitzell, E. Lonnoy, J.B.R. Matthews, T.K.*
918 *Maycock, T. Waterfield, O. Yelekçi, R. Yu, and B. Zhou (eds.)]*, Cambridge University Press. In Press, 2021.

919 Ivy-Ochs, S., Kerschner, H., Maisch, M., Christl, M., Kubik, P. W., and Schlüchter, C.: Latest Pleistocene and Holocene
920 glacier variations in the European Alps, *Quaternary Science Reviews*, 28, 2137–2149,
921 <https://doi.org/10.1016/j.quascirev.2009.03.009>, 2009.

922 Jäger, D. and Winkler, S.: Paraglacial processes on the glacier foreland of Vernagtferner (Ötztal Alps, Austria), *Zeit fur Geo*
923 *Supp*, 56, 95–113, <https://doi.org/10.1127/0372-8854/2012/S-00099>, 2012.

924 Jiménez, P. A., Dudhia, J., González-Rouco, J. F., Navarro, J., Montávez, J. P., and García-Bustamante, E.: A Revised
925 Scheme for the WRF Surface Layer Formulation, *Mon. Wea. Rev.*, 140, 898–918, <https://doi.org/10.1175/mwr-d-11->
926 00056.1, 2012.

927 Kain, J. S.: The Kain–Fritsch Convective Parameterization: An Update, *Journal of Applied Meteorology and Climatology*,
928 43, 170–181, [https://doi.org/10.1175/1520-0450\(2004\)043<0170:TKCPAU>2.0.CO;2](https://doi.org/10.1175/1520-0450(2004)043<0170:TKCPAU>2.0.CO;2), available at:
929 https://journals.ametsoc.org/view/journals/apme/43/1/1520-0450_2004_043_0170_tkcpau_2.0.co_2.xml, 2004.

930 Klein, G., Vitasse, Y., Rixen, C., Marty, C., and Rebetz, M.: Shorter snow cover duration since 1970 in the Swiss Alps due
931 to earlier snowmelt more than to later snow onset, *Climatic Change*, 139, 637–649, <https://doi.org/10.1007/s10584-016->
932 1806-y, 2016.

933 Lane, S., Bakker, M., Gabbud, C., Micheletti, N., and Saugy, J.-N.: Sediment export, transient landscape response and
934 catchment-scale connectivity following rapid climate warming and Alpine glacier recession, *Geomorphology*, 277, 210–
935 227, <https://doi.org/10.1016/j.geomorph.2016.02.015>, available at: <http://dx.doi.org/10.1016/j.geomorph.2016.02.015>,
936 2017.

937 Lane, S. N., Westaway, R. M., and Murray Hicks, D.: Estimation of erosion and deposition volumes in a large, gravel-bed,
938 braided river using synoptic remote sensing, *Earth Surf. Process. Landforms*, 28, 249–271,
939 <https://doi.org/10.1002/esp.483>, 2003.

940 Mair, V. and Purtscheller, F.: Exkursion E: Geologie und Petrologie des Ortlerkristallins, *Mitteilungen der Österreichischen*
941 *Mineralogischen Gesellschaft*, 285–303, 1996.

942 Mair, V., Nocker, C., and Tropper, P.: Das Ortler-Campo Kristallin in Südtirol, *Mitteilungen der Österreichischen*
943 *Mineralogischen Gesellschaft*, 219–240, 2007.

944 Mankin, J. S. and Diffenbaugh, N. S.: Influence of temperature and precipitation variability on near-term snow trends, *Clim*
945 *Dyn*, 45, 1099–1116, <https://doi.org/10.1007/s00382-014-2357-4>, 2015.

946 Matthews, J. A. and Briffa, K. R.: The ‘little ice age’: re-evaluation of an evolving concept, *Geografiska Annaler: Series A,*
947 *Physical Geography*, 87, 17–36, <https://doi.org/10.1111/j.0435-3676.2005.00242.x>, 2005.

948 Mattson, L. E. and Gardner, J. S.: Mass Wasting on Valley-Side Ice-Cored Moraines, *Boundary Glacier, Alberta, Canada,*
949 *Geografiska Annaler: Series A, Physical Geography*, 73, 123–128, <https://doi.org/10.1080/04353676.1991.11880337>,
950 1991.

951 Midgley, N. G. and Tonkin, T. N.: Reconstruction of former glacier surface topography from archive oblique aerial images,
952 *Geomorphology*, 282, 18–26, <https://doi.org/10.1016/j.geomorph.2017.01.008>, 2017.

953 Mölg, N. and Bolch, T.: Structure-from-Motion Using Historical Aerial Images to Analyse Changes in Glacier Surface
954 Elevation, *Remote Sensing*, 9, 1021, <https://doi.org/10.3390/rs9101021>, available at: <https://www.mdpi.com/228032>,
955 2017.

956 Morrison, H., Thompson, G., and Tatarskii, V.: Impact of Cloud Microphysics on the Development of Trailing Stratiform
957 Precipitation in a Simulated Squall Line: Comparison of One- and Two-Moment Schemes, *Mon. Wea. Rev.*, 137, 991–
958 1007, <https://doi.org/10.1175/2008MWR2556.1>, available at:
959 https://journals.ametsoc.org/view/journals/mwre/137/3/2008mwr2556.1.xml?tab_body=pdf, 2009.

960 Nebiker, S., Lack, N., and Deuber, M.: Building Change Detection from Historical Aerial Photographs Using Dense Image
961 Matching and Object-Based Image Analysis, *Remote Sensing*, 6, 8310–8336, <https://doi.org/10.3390/rs6098310>, 2014.

962 Neugirg, F., Kaiser, A., Huber, A., Heckmann, T., Schindewolf, M., Schmidt, J., Becht, M., and Haas, F.: Using terrestrial
963 LiDAR data to analyse morphodynamics on steep unvegetated slopes driven by different geomorphic processes,
964 *CATENA*, 142, 269–280, <https://doi.org/10.1016/j.catena.2016.03.021>, 2016.

965 Neugirg, F., Kaiser, A., Schmidt, J., Becht, M., and Haas, F.: Quantification, analysis and modelling of soil erosion on steep
966 slopes using LiDAR and UAV photographs, *Proc. IAHS*, 367, 51–58, 2015a.

967 Neugirg, F., Kaiser, A., Schindewolf, M., Becht, M., Schmidt, J., and Haas, F.: Monitoring and modeling slope dynamics in
968 an Alpine watershed - a combined approach of soil science remote sensing and geomorphology, *Proc. IAHS*, 371, 181–
969 187, 2015b.

970 Noto, L. V., Bastola, S., Dialynas, Y. G., Arnone, E., and Bras, R. L.: Integration of fuzzy logic and image analysis for the
971 detection of gullies in the Calhoun Critical Zone Observatory using airborne LiDAR data, *ISPRS Journal of*
972 *Photogrammetry and Remote Sensing*, 126, 209–224, <https://doi.org/10.1016/j.isprsjprs.2017.02.013>, 2017.

973 O'Callaghan, J. F. and Mark, D. M.: The extraction of drainage networks from digital elevation data. *Computer vision,*
974 *graphics, and image processing*, *Computer vision, graphics, and image processing*, 28, 323–344, 1984.

975 Okyay, U., Telling, J., Glennie, C. L., and Dietrich, W. E.: Airborne lidar change detection: An overview of Earth sciences
976 applications, *Earth-Science Reviews*, 198, 102929, <https://doi.org/10.1016/j.earscirev.2019.102929>, 2019.

977 Pelletier, J. D. and Orem, C. A.: How do sediment yields from post-wildfire debris-laden flows depend on terrain slope, soil
978 burn severity class, and drainage basin area? Insights from airborne-LiDAR change detection, *Earth Surf. Process.*
979 *Landforms*, 39, 1822–1832, <https://doi.org/10.1002/esp.3570>, 2014.

980 Pepin, N. C., Arnone, E., Gobiet, A., Haslinger, K., Kotlarski, S., Notarnicola, C., Palazzi, E., Seibert, P., Serafin, S.,
981 Schöner, W., Terzago, S., Thornton, J. M., Vuille, M., and Adler, C.: Climate Changes and Their Elevational Patterns in
982 the Mountains of the World, *Reviews of Geophysics*, 60, e2020RG000730, <https://doi.org/10.1029/2020RG000730>,
983 2022.

984 Piermattei, L., Heckmann, T., Betz-Nutz, S., Altmann, M., Rom, J., Fleischer, F., Stark, M., Haas, F., Ressler, C., Wimmer,
985 M., Pfeifer, N., and Becht, M.: Evolution of an Alpine proglacial river during seven decades of deglaciation quantified
986 from photogrammetric and LiDAR digital elevation models, *Earth Surf. Dynam. Discuss.* [preprint],
987 <https://doi.org/10.5194/esurf-2022-63>, 2022.

988 Pulighe, G. and Fava, F.: DEM extraction from archive aerial photos: accuracy assessment in areas of complex topography,
989 *European Journal of Remote Sensing*, 46, 363–378, <https://doi.org/10.5721/EuJRS20134621>, 2013.

990 Rieger, D.: Bewertung der naturräumlichen Rahmenbedingungen für die Entstehung von Hangmuren: Möglichkeiten zur
991 Modellierung des Murpotentials, vol. 51 of *Münchener Geographische Abhandlungen A*, Geobuch, München, 1999.

- 992 Rolstad, C., Haug, T., and Denby, B.: Spatially integrated geodetic glacier mass balance and its uncertainty based on
993 geostatistical analysis: application to the western Svartisen ice cap, Norway, *J. Glaciol.*, 55, 666–680,
994 <https://doi.org/10.3189/002214309789470950>, 2009.
- 995 Sass, O., Haas, F., Schimmer, C., Heel, M., Bremer, M., Stöger, F., and Wetzel, K.: Impact of forest fires on geomorphic
996 processes in the tyrolean limestone alps, *Geografiska Annaler: Series A, Physical Geography*, 94, 117–133,
997 <https://doi.org/10.1111/j.1468-0459.2012.00452.x>, 2012.
- 998 Schiefer, E. and Gilbert, R.: Reconstructing morphometric change in a proglacial landscape using historical aerial
999 photography and automated DEM generation, *Geomorphology*, 88, 167–178,
1000 <https://doi.org/10.1016/j.geomorph.2006.11.003>, 2007.
- 1001 Serquet, G., Marty, C., Dulex, J.-P., and Rebetez, M.: Seasonal trends and temperature dependence of the
1002 snowfall/precipitationday ratio in Switzerland, *Geophys. Res. Lett.*, 38, 14–18, <https://doi.org/10.1029/2011GL046976>,
1003 2011.
- 1004 Sevara, C., Verhoeven, G., Doneus, M., and Draganits, E.: Surfaces from the Visual Past: Recovering High-Resolution
1005 Terrain Data from Historic Aerial Imagery for Multitemporal Landscape Analysis, *J Archaeol Method Theory*, 25, 611–
1006 642, <https://doi.org/10.1007/s10816-017-9348-9>, available at: [https://link.springer.com/article/10.1007/s10816-017-](https://link.springer.com/article/10.1007/s10816-017-9348-9)
1007 9348-9, 2018.
- 1008 Skamarock, W. C. and Klemp, J. B.: A time-split nonhydrostatic atmospheric model for weather research and forecasting
1009 applications, *Journal of Computational Physics*, 227, 3465–3485, <https://doi.org/10.1016/j.jcp.2007.01.037>, 2008.
- 1010 Slivinski, L. C., Compo, G. P., Whitaker, J. S., Sardeshmukh, P. D., Giese, B. S., McColl, C., Allan, R., Yin, X., Vose, R.,
1011 Titchner, H., Kennedy, J., Spencer, L. J., Ashcroft, L., Brönnimann, S., Brunet, M., Camuffo, D., Cornes, R., Cram, T.
1012 A., Crouthamel, R., Domínguez-Castro, F., Freeman, J. E., Gergis, J., Hawkins, E., Jones, P. D., Jourdain, S., Kaplan,
1013 A., Kubota, H., Le Blancq, F., Lee, T.-C., Lorrey, A., Luterbacher, J., Maugeri, M., Mock, C. J., Moore, G. K.,
1014 Przybylak, R., Pudmenzky, C., Reason, C., Slonosky, V. C., Smith, C. A., Tinz, B., Trewin, B., Valente, M. A., Wang,
1015 X. L., Wilkinson, C., Wood, K., and Wyszyński, P.: Towards a more reliable historical reanalysis: Improvements for
1016 version 3 of the Twentieth Century Reanalysis system, *Quarterly Journal of the Royal Meteorological Society*, 145,
1017 2876–2908, <https://doi.org/10.1002/qj.3598>, 2019.
- 1018 Smith, M. W., Carrivick, J. L., and Quincey, D. J.: Structure from motion photogrammetry in physical geography, *Progress*
1019 *in Physical Geography: Earth and Environment*, 40, 247–275, <https://doi.org/10.1177/0309133315615805>, 2016.
- 1020 Staindl, A.: *Kurze Geologie von Südtirol*, Weger, Brixen, 2000.
- 1021 Stark, M., Rom, J., Haas, F., Piermattei, L., Fleischer, F., Altmann, M., and Becht, M.: Long-term assessment of terrain
1022 changes and calculation of erosion rates in an alpine catchment based on SfM-MVS processing of historical aerial
1023 images. How camera information and processing strategy affect quantitative analysis, *jgeomorphology*,
1024 <https://doi.org/10.1127/jgeomorphology/2022/0755>, 2022.

- 1025 Tarolli, P.: High-resolution topography for understanding Earth surface processes: Opportunities and challenges,
1026 *Geomorphology*, 216, 295–312, <https://doi.org/10.1016/j.geomorph.2014.03.008>, 2014.
- 1027 Tollmann, A.: *Geologie von Österreich: Die Zentralalpen*, Deuticke, Wien, 1977.
- 1028 Vehling, L.: *Gravitative Massenbewegungen an alpinen Felshängen: Quantitative Bedeutung in der Sedimentkaskade*
1029 *proglazialer Geosysteme (Kaunertal, Tirol)*, Doctoral thesis, Friedrich-Alexander-Universität Erlangen-Nürnberg,
1030 Erlangen, 2016.
- 1031 Veit, H.: *Die Alpen: Geoökologie und Landschaftsentwicklung*, Ulmer, Stuttgart, 2002.
- 1032 Wester, T., Wasklewicz, T., and Staley, D.: Functional and structural connectivity within a recently burned drainage basin,
1033 *Geomorphology*, 206, 362–373, <https://doi.org/10.1016/j.geomorph.2013.10.011>, available at:
1034 <http://www.sciencedirect.com/science/article/pii/S0169555X13005242>, 2014.
- 1035 Zhong, Y., Liu, Q., Westoby, M., Nie, Y., Pellicciotti, F., Zhang, B., Cai, J., Liu, G., Liao, H., and Lu, X.: Intensified
1036 paraglacial slope failures due to accelerating downwasting of a temperate glacier in Mt. Gongga, southeastern Tibetan
1037 Plateau, *Earth Surf. Dynam.*, 10, 23–42, <https://doi.org/10.5194/esurf-10-23-2022>, 2022.
- 1038